Heavy element abundances in the second parameter globular cluster pair NGC288/362

NGC 288

Master of Science Thesis in Astronomy

Paul Anthony Wilson

Supervisors:
David Yong, Frank Grundahl and Mats Carlsson

Heavy element abundances in the second parameter globular cluster pair NGC288/362

Paul Anthony Wilson

Institute of Theoretical Astrophysics
UNIVERSITY OF OSLO
Oslo, Norway, 2010

Heavy element abundances in the second parameter globular cluster pair NGC288/362

Institute of Theoretical Astrophysics
University of Oslo
P.O. Box 1029 Blindern
N-0315 Oslo
Norway
Telephone: +47 22 85 65 01

Institute of Theoretical Astrophysics, Oslo, 2010

Cover illustration: Paul Anthony Wilson, taken with the Nordic Optical Telescope.

In loving memory of my father,

Anthony Berry Wilson.

ABSTRACT

The aim of this thesis is to measure and assess the relative abundance ratios of heavy elements (Si to Eu) in the second parameter pair NGC 288 and NGC 362. The results serve as upper limits on the element abundances in the two clusters. This is needed in the context of the 2nd parameter problem which, as of yet, does not have a satisfactory solution. Studies such as the one presented in this thesis are important for providing constraints upon the uniformity of mixing in the proto-cluster environment and for constraining the role of heavy element abundance as a 2nd parameter candidate.

The observations were done in 2005 using the Very Large Telescope (VLT[1]) together with the UVES[2] spectrograph (Dekker et al. 2000). The study contains 8 stars in NGC 288 and 8 stars in NGC 362. The abundances of 15 heavy elements are reported for the two clusters, including the s-process elements Y, Zr, Ba, La and Ce and r-process element Eu. The abundances were derived using two separate and independent techniques: The Spectroscopic Approach, where the atmospheric models were based on initial guesses of effective temperature ($T_{\rm eff}$) and gravity ($\log(g)$) as input parameters; and the Photometric Approach, where empirical formulae were used. Using the latter approach the $T_{\rm eff}$was calculated using metallicity-dependent temperature vs. colour calibrations based on temperatures derived using the infrared flux method (IRFM) (Blackwell & Shallis 1977), and the $\log(g)$ was calculated using standard formulae which require estimates of effective temperature, mass, distance and magnitudes.

The results show that the [X/Fe] ratios in NGC 288 are considerably higher than in NGC 362. This is presumably due to the different [Fe/H] derived for NGC 362. The exceptions to this difference between the clusters are Mn (affected by hyperfine structure splitting), Ba (affected by hyperfine structure and isotopic splitting). Hyperfine structure splitting and isotopic splitting have not been taken into account in this thesis. Thus, results would suggest that NGC 362 formed from material with a higher concentration of r-process products than NGC 288. Removing the [Fe/H] dependence, the abundance differences between the clusters decrease. [X/H] ratios shows that NGC 362 has a higher abundance than NGC 288, which is opposite to the [X/Fe] case.

[1]Located on Cerro Paranal in the Atacama Desert, northern Chile.
[2]Ultraviolet and Visual Echelle Spectrograph

CONTENTS

1 INTRODUCTION **1**

2 OBSERVATIONS **3**

3 ANALYSIS **5**

3.1 The Spectroscopic Approach 5

3.1.1 The parameters 9

3.2 The Photometric Approach 11

3.2.1 $T_{\rm eff}$ 11

3.2.2 $\log(g)$ 12

4 RESULTS **15**

4.1 Abundances from the spectroscopic approach 15

4.2 Abundances from the photometric approach 20

4.3 Abundance dependencies on model parameters 24

4.4 Predicted and observed scatter in abundance ratios 25

4.5 Result Comparison 26

4.5.1 Comparison between the clusters 26

4.5.2 Comparison between the spectroscopic and photometric approach 30

4.5.3 Comparison with other results in literature 32

5 DISCUSSION **35**

5.1 Abundances 35

5.1.1 [Fe I/H] and [Fe II/H] 35

5.1.2 α Elements 36

5.1.3 Fe-peak elements 37
5.1.4 Neutron-Capture Elements 38
5.1.5 The s-process elements 39
5.1.6 The r-process elements 39
5.1.7 The p-process elements 40
5.2 Comparison of the spectroscopic and photometric approach 41
5.2.1 The preferred approach 41
5.2.2 Constraints on the abundance differences between the clusters. 42
5.3 Errors 43
5.3.1 Model atmospheres 43
5.3.2 EW measurements and the curve of growth 44
5.3.3 Error budget 48
5.3.4 NLTE effects 50
5.3.5 Results in the context of the second parameter problem 50
5.3.6 Future work 51

6 CONCLUSION **52**

APPENDIX **52**

A Adopted Solar Abundances **53**

B Abundance calculations **55**
B.0.7 $\log \varepsilon(X)$ notation 55
B.0.8 "Bracket notation" 55

1 INTRODUCTION

Globular clusters (GCs) are built up of a vast collection of gravitationally bound stars. Found in the disk and the halo of our galaxy these intrinsically bright objects have helped astronomers understand and verify stellar nucleosynthesis and stellar evolutionary theories. Containing a large population of stars thought to have similar ages and to be located at virtually the same distance from us, GC work well as a cosmic laboratory for studying the different phases of a star's life (Gratton et al. 2004). GCs are also used to probe the ages of the oldest stars since it is very difficult to determine the age of individual stars with good accuracy. Age determinations, of increasing accuracy, are possible from measurements of the radioactive decay of Th and/or U relative to other r-process elements. Although GCs have been carefully studied for decades and great progress has been made in understanding them, there are still a number of peculiarities and properties of GCs which have not been fully understood or explained. One such peculiarity is the second parameter effect, which will be explained below.

The location of the horizontal branch (HB) in the HR[1] diagram is most strongly influenced by the metallicity ([Fe/H]) of the cluster (Sandage & Wildey 1967), (Dotter et al. 2010). The metallicity of the cluster is, however, not by itself sufficient in explaining the different HB morphologies various GCs exhibit. Thus, clusters which have similar metallicities, yet different HB locations, must be affected by at least one, but more likely several other parameters. It is these other parameters which are referred to as *"the second parameter"*. The search for the second parameter has lead to a number of different theories. It is, however, worth noting that, although there are a number of second parameter candidates, it is not certain which candidate is primarily dominating the location of the HB after metallicity, the first parameter. One of the more common of these second parameter candidates is the age difference between clusters (Rood 1973), (Demarque et al. 1989), where older more metal poor clusters tend to have a bluer HB. Furthermore, Catelan et al. (2001) suggested that there is a correlation between the central density of globular clusters and mass dispersion on the HB. This is presumably related to the way a dense environment is able to affect mass loss on the Red Giant Branch (RGB). However, to be able to determine this scenario, a deeper understanding of the mass-loss process in red giant stars is needed in order to reach a conclusive answer. Currently there is no accurate description of how dense stellar media might contribute to the occurrence of increased mass loss and thus to a bluer HB morphology. Another second parameter candidate is the variation of helium in the envelopes of the stars in the GCs (D'Antona et al. 2002), which affect their hydrogen burning lifetimes. However, since it is difficult to estimate the abundance of He observationally, there still is a great uncertainty in the effect this would have as a second parameter.

In this thesis, the heavier elements of what is probably the best known "second-

[1]Hertzsprung-Russel diagram

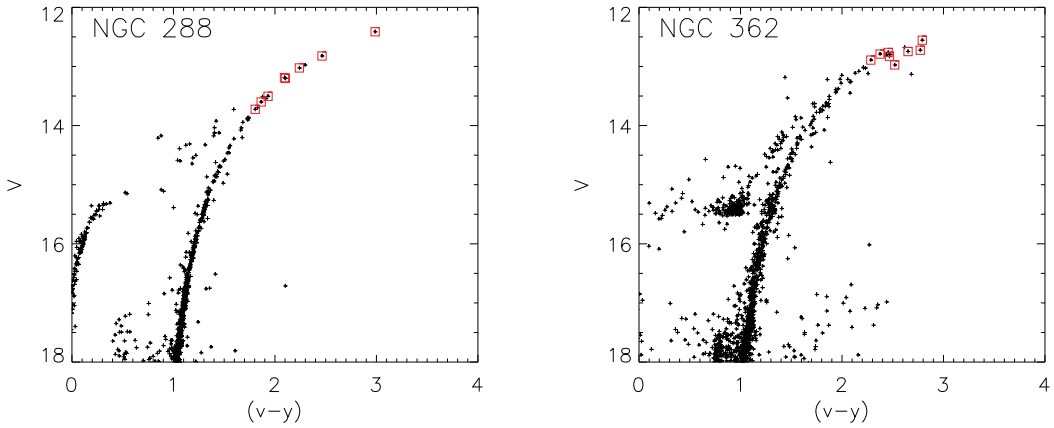

Figure 1.1 Colour Magnitude Diagram (CMD) of NGC 288 and NGC 362. Shown here are the very distinctly separate HBs. The red squares indicate the stars used in this thesis.

parameter pair", NGC 288 and NGC 362, have been studied (Catelan et al. 2001). This second parameter pair has two very distinct HB morphologies, as seen in Figure 1.1. NGC 288 is seen to have a much bluer HB than NGC 362.

The spectra are the highest quality spectra[2] ever obtained for NGC 288 and NGC 362 (R=110,000, S/N=150)[3]. With these spectra, the main goal of the thesis is to measure the most accurate and precise relative abundance ratios for heavy elements in these clusters. By comparing the relative abundance ratios within and between these two key clusters a suggestion of new constraints on the abundance differences between these clusters can be found.

In this thesis an abundance analysis of 15 heavy elements in 16 of the brightest stars in NGC 288 and NGC 362 was done. The analysis was based on high signal to noise high resolution spectra obtained using UVES at the VLT. The wavelength region from about 4800 Å to 6800 Å has been chosen, as most iron lines are found in this region for RGB stars. As seen in figure, 1.1 the brightest stars were chosen. Stars on the HB were not observed as there exist abundance anomalies, which arise from metal levitations (Grundahl et al. 1999) and diffusion processes such as He diffusion. In the case where the outer envelope is stable enough for the gravitational settling of He to be efficient, heavy element overabundances are produced (Michaud et al. 1983). Despite this, if spectra were to be taken to obtain the same signal to noise level, much more observing time would be needed. If using the same resolution setting on UVES, observation time of the stars on the HB would have to be increased by a minimum factor of about $\sim$ 4. This would amount to about 150 hours of telescope time at the VLT, which would not be allotted to such a project.

[2]within the wavelength region from approximately 4800 Å to 6800 Å

[3]See 2 for an explanation on why such high quality data was used. S/N is about 150 per pixel at a wavelength of 5000 Å

2 OBSERVATIONS

The sample consists of 16 RGB stars where 8 are located in NGC 288 and 8 in NGC 362. Observations[1] were done using the UVES Echelle spectrograph at the VLT mounted at the Nasmyth B focus of UT2[2]. UVES is a cross-dispersed echelle spectrograph covering a wavelength region between the atmospheric cut-off at 300 nm and the long wavelength limit of the CCD detectors at 1100 nm. The wavelength range sampled went from 4760 Å to 6830 Å. The wavelength region was chosen primarily because of the observation program ID 075.D-0209(A), where the data will be used in order to measure the Mg isotope ratios. The wavelength region from 4760 Å to 6830 Å is suitable for this, as it covers the 514 nm MgH lines needed. The wavelength region is also useful as the line density gives a lot of spectral lines without the region being too overcrowded.

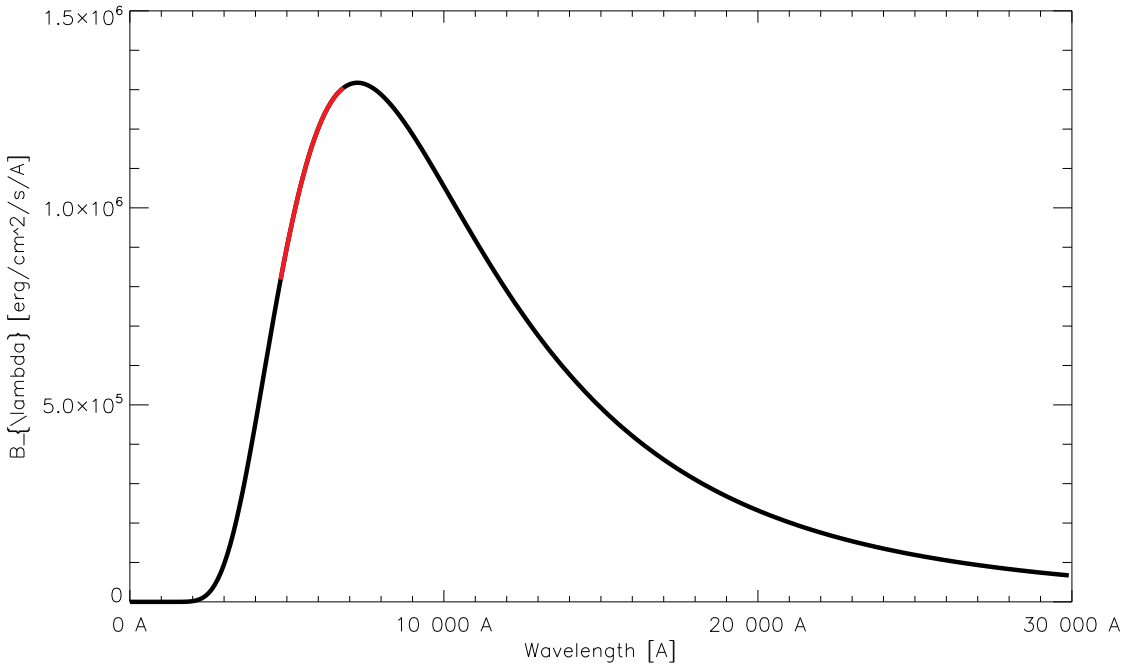

Figure 2.1 Planck function for a star with $T_{\rm eff}$= 4000 K. The wavelength range studied is marked in red.

The light beam from the telescope is split in two arms within the instrument: one covering the bluer wavelengths, and the other the redder wavelengths. The light from the red-arm ends up on two detectors each of which cover the wavelengths (4760 Å to 5750 Å) and (5830 Å to 6830 Å). An image slicer was employed which in turn allowed for less strict constraints upon the seeing conditions. The image slicer also enabled the observations to be done using the smallest slit (ensuring the highest

[1]ESO program ID: ID 075.D-0209(A), PI: Grundahl, F.
[2]Unit Telescope 2, Kueyen

specral resoltion), whilst minimising the slit loss. The exposure time for each star was in the order of 3000 seconds. Image slicer #3 was used, which has a slit width of 0.30 arcseconds and a height of 10 arcseconds. The signal to noise ranged between 140 to 150 depending on the brightness of the star and the wavelength region.

The spectra were reduced using the standard ESO UVES pipeline. The spectra were further continuum normalised using the DAOSPEC package[3], which is a Fortran program that automatically finds absorption lines in a stellar spectrum, fits the continuum, measures equivalent widths, and identifies lines with a laboratory line list. The equivalent width measurements were done using an IRAF cl script that fits a Gaussian to each line. Examples of such fits are seen in Figures 3.2 and 3.3. This was a semi-automated process which had to fit three criteria for the line to be accepted. The first criterium was the minimum line strength, the second the maximum line strength and the third the maximum velocity offset. These criteria were set to try and avoid measuring noise and weak lines, to avoid very strong lines, and to avoid lines with the incorrect wavelength. Each line was later checked visually to ensure a good fit was made, as shown in Figure 3.3.

[3]http://www1.cadc-ccda.hia-iha.nrc-cnrc.gc.ca/community/STETSON/daospec/

3 ANALYSIS

The heavy element abundances were found using two different approaches: the spectroscopic approach and the photometric approach. This was done in order to have two ways of independently verifying the results.

3.1 The Spectroscopic Approach

The spectroscopic approach involved using the obtained spectra directly. The equivalent widths (EWs) of the spectral lines were measured, and then used together with stellar atmosphere models to derive elemental abundances for the different elements. The stellar parameters were determined using a traditional spectroscopic approach, which will now be described. The EWs from the spectral absorption lines, from each element studied, was measured using IRAF[1]. Having measured the equivalent widths, stellar atmosphere models were created using Kurucz models (Kurucz 1993), assuming local thermodynamic equilibrium (LTE). An interpolated model was used when necessary. The stellar parameters required for the abundance analysis were effective temperature ($T_{\rm eff}$), gravity ($\log(g)$), and micro turbulent velocity (ξ_t). The initial guesses of these values are from Shetrone & Keane (2000). Alonso et al. (1999*a*) and Ramírez & Meléndez (2005) give IRFM calibrations from which additional estimates were obtained. The LTE stellar line analysis program MOOG (Sneden 1973) was used together with the EWs and the Kurucz LTE model atmospheres to determine the abundances for a given line. Since MOOG assumes local thermodynamic equilibrium (LTE), the level populations of the model atmosphere's 72 layers are governed by the local temperature.

The objective is to create an atmospheric model which, when put into MOOG, gives an Fe I abundance as close to an Fe II abundance as possible. To achieve this, the input parameters of the Kurucz model were changed iteratively. By changing the model parameters, the different element abundances were calculated using MOOG. The equivalent widths of the Fe I and Fe II lines were used in order to create a 1-D stellar atmosphere model. The effective temperature $T_{\rm eff}$, was changed iteratively until there was no trend between the abundances from the Fe I lines[2] ($\log\epsilon$(Fe I)) and the lower excitation potential (Figure 3.1). The presence of a trend indicated whether the $T_{\rm eff}$ was too low or too high. The surface gravity $\log(g)$ was found by making the Fe I and Fe II abundances the same. The micro turbulent velocity ξ_t was adjusted until there was no trend between the Fe I abundances and the EWs.

[1]IRAF (Image Reduction and Analysis Facility) is distributed by the National Optical Astronomy Observatory which is operated by the Association of Universities for Research in Astronomy, Inc., under contract with the National Science Foundation.

[2]log(eps(Fe I)) =logϵ(Fe I) = $\log_{10}\left(\frac{N_{\rm FeI}}{N_{\rm H}}\right)_{star}$

Changing the value of $\log(g)$ and ξ_t would effect the trend between the abundances from the Fe I lines and the lower excitation potential, making it necessary to once again change the value of $T_{\rm eff}$. Changing the value of $T_{\rm eff}$ would then again make it necessary to slightly alter the other parameters. Thus, the process of finding self-consistent stellar parameters was done through many iterations, as all the parameters are coupled in a non-linear fashion. The ideal model would in the end neither have a trend between the Fe I abundance and lower excitation potential, nor between the Fe I abundance and the EWs. Also the model would have to have both $\log\epsilon$(Fe I) and $\log\epsilon$(Fe II) equal to each other.

The different parameters all effect the slopes of these graphs. Points that seemed to effect the slopes greatly, and did not seem to follow the general trend, were in most cases removed or checked again by manually measuring the equivalent widths. If the measurement was affected by cosmic ray spikes, or the line had a bad continuum, and so forth, the EW measurement of the line was not used, see Figure 3.2. The removal of such lines together with the removal of abundances which differed greatly from the mean lead to a more accurate abundance determination. However, by removing or remeasuring the EWs, the abundances once again changed, making it necessary to once more adjust the parameters.

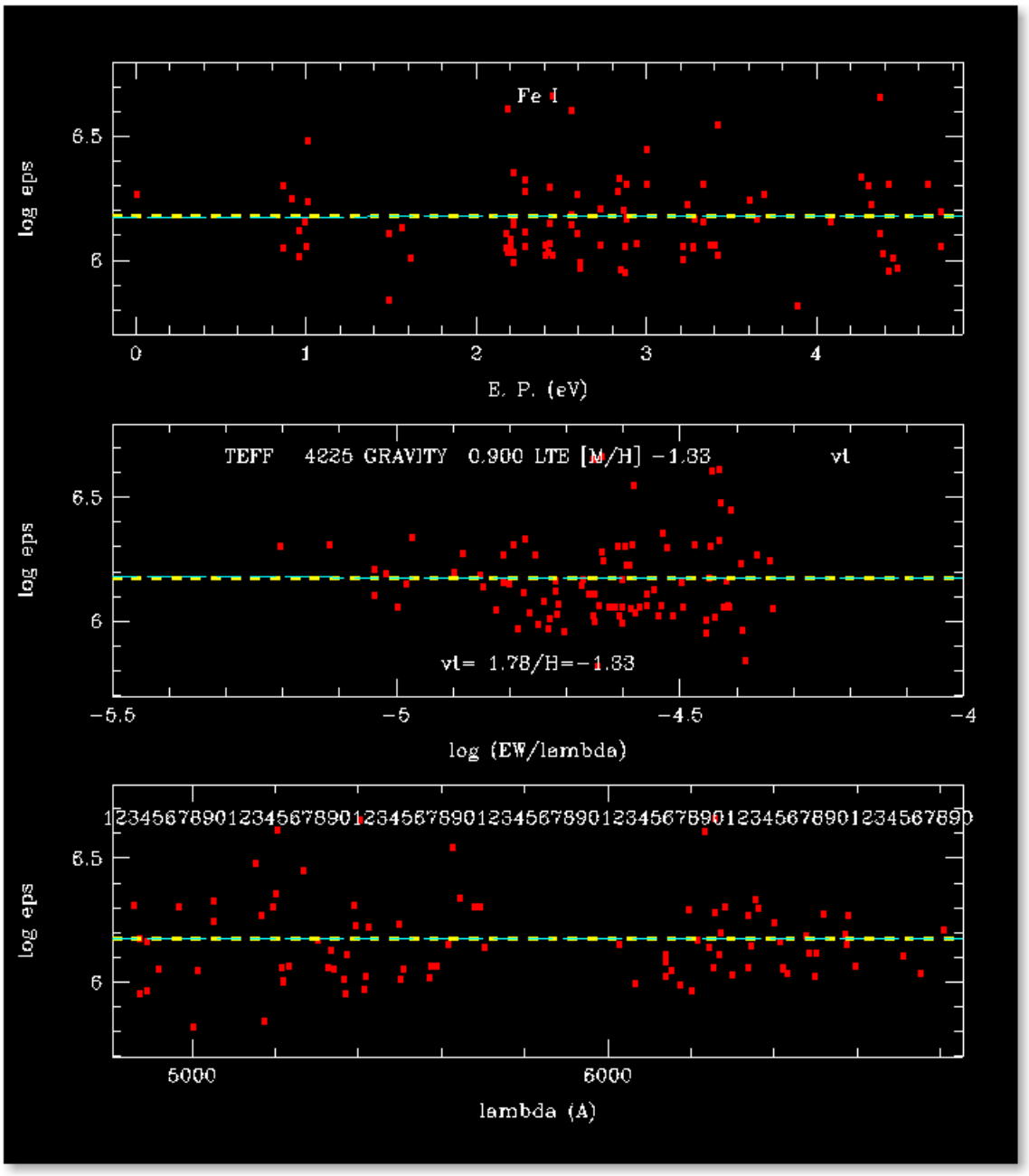

Figure 3.1 The graphical MOOG output for the star NGC288-344 showing 3 plots. First plot is $\log \epsilon$ vs excitation potential. This graph was used to iteratively find $T_{\rm eff}$ by having the slope equal to zero. The next plot is $\log \epsilon$ vs reduced equivalent width ($\log W/\lambda$), which together with the plot above helps in the determination of ξ_t, by having both slopes set to zero. The last graph $\log \epsilon$ vs wavelength (λ), is useful as an overview of scatter as a function of wavelength. Notice how the light from the red-arm ends up on two detectors creating a separate blue and red region of scatter.

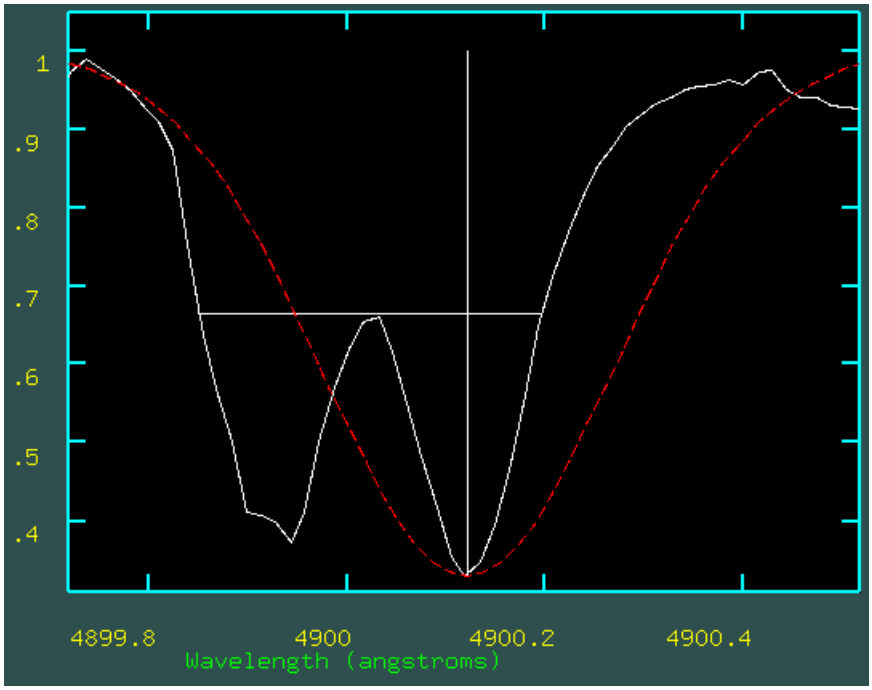

Figure 3.2 An example of a poor fit. Two closely spaced absorption lines throw off the automated EW measurements. Such lines were not included when calculating the abundances.

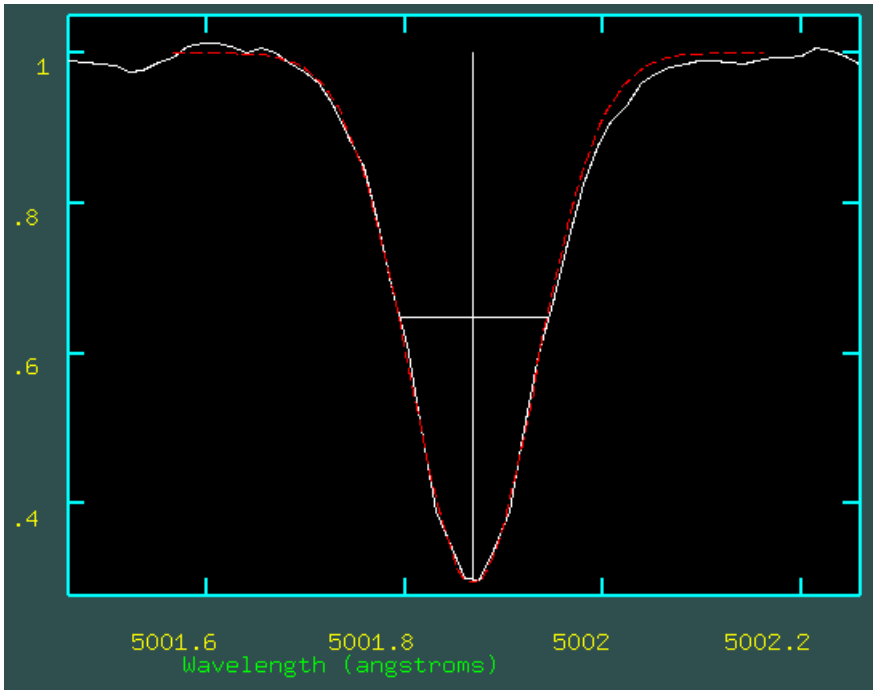

Figure 3.3 An example of a good gaussian fit.

3.1.1 The parameters

$T_{\rm eff}$ – Effective Temperature

Effective temperature is the most important parameter when determining chemical abundances. In the spectroscopic approach, an incorrect $T_{\rm eff}$ is apparent when there are trends between abundance and the lower excitation potential. The temperature was adjusted in steps of about 25 K until the abundances from the Fe I lines displayed no trends with the lower excitation potential. Then, once the other parameters also had changed very slightly, alterations to the temperature on the 5 K scale were made. $T_{\rm eff}$ is the parameter which has the biggest effect on the abundances of the Fe I lines. The population density ratio, and thus the abundance, is largely temperature dependant as seen by the Boltzmann Equation:

$$\frac{N_b}{N_a} = \frac{g_b}{g_a} e^{-(E_b - E_a)/kT} \tag{3.1}$$

Here N_a and N_b give the number of excited atoms, whilst E_a and E_b are the energies of the different states. The statistical weights g_a and g_b give the number of states with energies E_a and E_b respectively. k is Boltzmann constant and T is the temperature. It is seen that, as the temperature increases, the Boltzmann factor ($e^{-(E_b-E_a)/kT}$) decreases and so there exist more atoms with a higher energy state. It was assumed that the excitation equilibrium was satisfied when the slope between $\log \epsilon$(Fe I) and lower excitation potential was ≤ 0.005.

$\log(g)$ – Gravity

The gravity is a parameter which mainly affects the electron pressure (P_e), which again affects the ratio between neutral atoms NI, and singly ionized atoms NII. The Saha Equation shows the relative populations of any two adjacent ionisation states. Choosing the ionisation states NI and NII, the Saha Equation takes the form:

$$\frac{N_{\rm II}}{N_{\rm I}} = \frac{2kTZ_{\rm II}}{P_e Z_{\rm I}} \left(\frac{2\pi m_e kT}{h^2} \right)^{3/2} e^{-\chi_{\rm I}/kT} \tag{3.2}$$

Here ZI and ZII are the partition functions, which are the weighted sums over energy states with different energies. The mass of the electron is expressed as m_e, and The Planck constant as h. $\chi_{\rm I}$ is the ionisation energy of the neutral atom. For a constant temperature it is seen that $\ln[N_{\rm II}/N_{\rm I} \times P_e] \propto$ constant. Thus, if P_e decreases, then the ratio $N_{\rm II}/N_{\rm I}$ increases, leading to more atoms in the singly ionized state NII. The gravity parameter was adjusted in steps of 0.05 dex[3] until the Fe I and Fe II lines were in agreement by having the average Fe I abundance as equal to the input

[3]dex, is a logarithmic unit were 1 dex equals a factor of 10. Example: 1 dex $= 10^1 = 10$.

abundance of the Fe II as possible. An increase in $\log(g)$ gave an increase in the average abundance of Fe II. It was assumed that the ionisation equilibrium was satisfied when $|\log\epsilon(\mathrm{Fe\,I}) - \log\epsilon(\mathrm{Fe\,II})| \leq 0.02$ dex.

ξ_t – Microturbulent velocity

The micro turbulent velocity was adjusted in steps of 0.01 km s^{-1}. The equivalent widths of the spectral lines (especially the strong ones) are affected by micro turbulent velocity, which again affects the abundances calculated. The strong absorption lines are caused by photons being absorbed close to the surface were the micro turbulent velocity is the strongest. A satisfactory micro turbulent velocity was determined when the slope between $\log\epsilon(\mathrm{Fe\,I})$ and the reduced equivalent width ($\log W/\lambda$) was ≤ 0.005.

$[Fe/H]$ – Metallicity

The metallicity of the clusters as found in Harris (1996) were used as a starting point. The input abundance of the Fe I lines were fine-tuned by changing the metallicity.

3.2 The Photometric Approach

The spectroscopy method above requires initial guesses for both $T_{\rm eff}$ and $\log(g)$ as input parameters. Subsequent iteration is usually required to obtain the final parameters, however, with the photometric approach, no further model iterations were done. If further model iterations were done, the parameters would most likely be very similar to the spectroscopic approach. The uncertainties associated with these parameters will directly have an effect on the element abundances. Thus, obtaining accurate $T_{\rm eff}$ and $\log(g)$ is a crucial step in this approach. $T_{\rm eff}$ and $\log(g)$ are quantities that can not be observed directly for distant globular cluster giants.

3.2.1 $T_{\rm eff}$

To be able to calculate a value for $T_{\rm eff}$, metallicity-dependent giant-star temperature vs. colour calibrations by Ramírez & Meléndez (2005) were used. These calibrations were based on main sequence and giant stars with temperatures derived using the infra-red flux method (IRFM) (Blackwell & Shallis 1977). The program stars of NGC 288 and NGC 362 fit well within the spectral range (F0 to K5), and the metallicity range of the colour-temperature relations ($-3.5 \gtrsim [Fe/H] \gtrsim 0.4$). By using a two step process where both metallicity and colour magnitudes are given as input parameters, the effective temperature was found using empirical equations from Ramírez & Meléndez (2005).

$$\theta_{eff} = a_0 + a_1 X + a_2 X^2 + a_3 X[\mathrm{Fe/H}] + a_4[\mathrm{Fe/H}] + a_5[\mathrm{Fe/H}]^2 \tag{3.3}$$

were $\theta_{eff} = 5040/T_{\rm eff}$. Here X represents the colour, and a_i $(i = 1, \ldots, 5)$ the coefficients of the fit. The metallicity used was adopted from Harris (1996). The photometry was provided by Frank Grundahl[4], and $T_{\rm eff}$ was derived from the $V-K$ colours. Corrections for interstellar reddening was taken into account using the following relation:

$$E(V-K) = E(B-V) \times 2.695 \tag{3.4}$$

Tables 3.1 and 3.2 show the photometric values obtained. The mass of the stars are assumed to be $m = 0.83 M_{\odot}$, which is a reasonable mass based on 13 Gyr isochrones (VandenBerg et al. 2006). The foreground reddening is assumed to be $E(B-V) = 0.03$, the $V-K$ reddening to be $E(V-K) = 0.08085$, and the apparent visual distance modulus $(m-M)_V = 14.65$ pc. $m = 0.83 M_{\odot}$ was chosen as it is a typical mass for the RGB program stars. The V magnitudes were provided by Frank Grundahl, and the K magnitudes are from the 2MASS survey. The value of $E(B-V)$ and distance modulus are from Harris (1996).

[4]ESO program ID: ID 075.D-0209

Table 3.1 Photometric values for NGC 288. $V-K$ is the colour and V is the visual magnitude of the star.

Star	V	$V-K$	$(V-K)_{corr}$
531	12.413	3.824	3.743
403	12.823	3.486	3.405
20C	13.025	3.255	3.174
281	13.190	3.179	3.098
344	13.201	3.126	3.045
338	13.601	2.927	2.846
351	13.504	2.951	2.870
287	13.725	2.868	2.787

Table 3.2 Photometric values for NGC 362. $V-K$ is the colour and V is the visual magnitude of the star.

Star	V	$V-K$	$(V-K)_{corr}$
1401	12.556	3.856	3.721
1423	12.748	3.644	3.509
1334	13.827	3.498	3.363
1441	13.725	3.690	3.555
1137	13.790	3.410	3.275
77	13.975	2.473	2.338
MB2	13.763	2.296	2.161
2127	13.892	2.315	2.180

The second step was to add the polynomial fits to Equation 3.5 where $P(X,[\mathrm{Fe/H}]) = P_0 + P_1X + P_2X^2 + P_3X[\mathrm{Fe/H}] + P_4[\mathrm{Fe/H}] + P_5[\mathrm{Fe/H}]^2$. Neglecting the polynomial fitting in Equation 3.5 would lead to systematic errors of the order of 30 K or 40 K (Ramírez & Meléndez 2005). The effective temperature is given by:

$$T_{\mathrm{eff}} = \frac{5040}{\theta_{eff}} + P(X,[\mathrm{Fe/H}]) \tag{3.5}$$

The results from these calculations can be found in Table 4.11 and 4.12 in Section 4.

3.2.2 $\log(g)$

Physical gravity

The physical gravity of the star $\log(g)$ was calculated from first principles using a few well known astronomical equations:

Newton's law of gravity:

$$g = \frac{GM}{R^2}, \tag{3.6}$$

Stefan-Boltzmann equation:

$$L = 4\pi R^2 \sigma T_{\rm eff}^4, \tag{3.7}$$

and

Magnitude luminosity equation:

$$\mathfrak{m} - \mathcal{M}_\odot = 2.5 \log \left(\frac{L_\odot}{L} \right), \tag{3.8}$$

By rewriting equation 3.7 as function of R^2 and substituting this into Equation 3.6 gives:

$$g = GM \left(\frac{4\pi\sigma T_{\rm eff}^4}{L} \right), \tag{3.9}$$

By dividing equation 3.9 for the star by the same equation for the sun gives:

$$\frac{g}{g_\odot} = \frac{M}{M_\odot} \cdot \frac{L_\odot}{L} \cdot \left(\frac{T_{\rm eff}}{T_{\rm eff\odot}} \right)^4, \tag{3.10}$$

rewriting equation 3.8 as

$$0.4(\mathfrak{m} - \mathcal{M}_\odot) = \log \frac{L_\odot}{L}, \tag{3.11}$$

and substituting this into Equation 3.10, of which the logarithm is taken, together with the bolometric correction,

$$BC = \mathcal{M}_V - \mathcal{M}_{\rm bol}, \tag{3.12}$$

where $\mathcal{M}_V$ is the visual magnitude and $\mathcal{M}_{\rm bol}$ is the bolometric magnitude of the star, gives:

$$\log(g) = 0.4(\mathcal{M}_V + BC - \mathcal{M}_{\odot Bol}) + \log(g_\odot) + 4 \log \frac{T_{\rm eff}}{T_{\rm eff\odot}} + \log \frac{M}{M_\odot}. \tag{3.13}$$

The stellar mass, M was assumed to be $0.83 M_\odot$ (low gravity stars). The value of the bolometric magnitude of the sun ($M_{\odot Bol}$), 4.75, was adopted from Cox & Pilachowski (2000). The absolute magnitude was calculated using the apparent visual distance modulus $\mathcal{M}_V = \mathfrak{m}_V - (\mathfrak{m} - \mathcal{M}_\odot)_V$, where the value for $(\mathfrak{m} - \mathcal{M}_\odot)_V$ is from Harris (1996). The bolometric correction value (BC) of the sun was adopted from Alonso et al. (1999*b*), who developed a transformation of the luminosity axis of theoretical isochrones into observational $\mathfrak{m}_V$ of colour-magnitude diagrams.

For stars in the range $3.56 \leq \log(T_{\rm eff}) \leq 3.67$ for $-0.5 \geq [\mathrm{Fe/H}] > -1.5$,

$$BC(V) = \frac{-5.531 \times 10^{-2}}{X} - 0.6177 + 4.420X - 2.669X^2 + 0.6943X[\mathrm{Fe/H}] - 0.1071[\mathrm{Fe/H}] - 8.612 \times 10^{-3}[\mathrm{Fe/H}]^2 \tag{3.14}$$

$\sigma(BC(V)) = 0.024$, (285 stars)

It is worth mentioning that another way of getting $\log(g)$ is possible by studying isochrones. By looking at the Y^2 isochrones (Demarque et al. 2004) and interpolating in metallicity and temperature a value for $\log(g)$ could be attained. More on the accuracy of the $\log(g)$ values are found in Section 5.2.

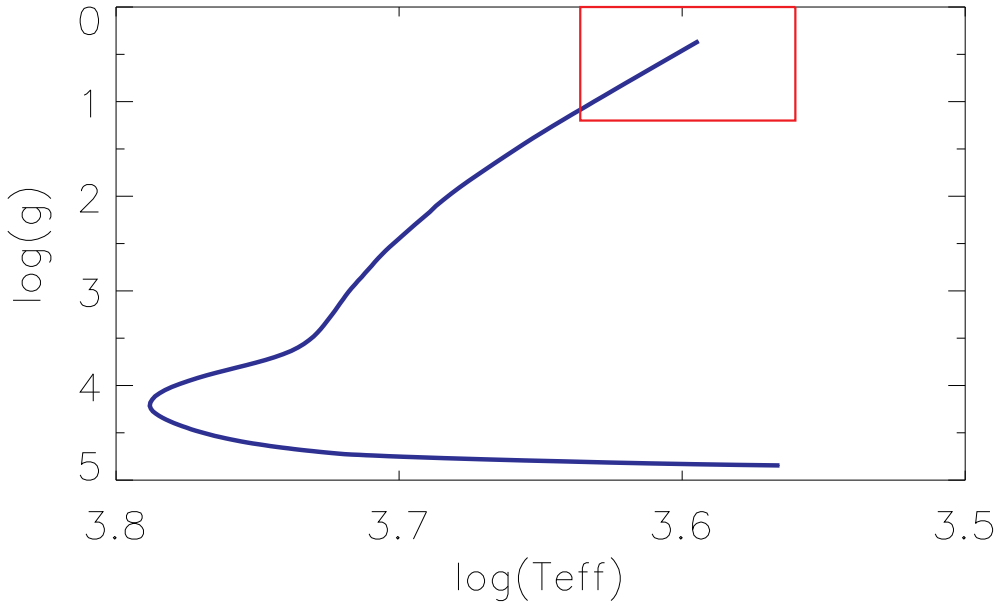

Figure 3.4 Y^2 isochrone with $Z = 0.001$, $Y = 0.232$, [Fe/H]$= -1.505247$, [α/Fe]$=$ 0.30 and AGE $=$ 13.0 Gyr. The red box marks the parameter area of the models.

4 RESULTS

The [Fe/H] abundances are throughout the thesis the same as the [Fe I/H] abundances. The adopted solar abundances are found in the Appendix, Section **??**. The error in the mean was calculated assuming a normal distribution, $\sigma/\sqrt{n}$.

4.1 Abundances from the spectroscopic approach

NGC 288

Overall average metallicity is found to be [Fe/H] = -1.40 ± 0.02. This value is obtained by not including the stars 531 and 287 as their [X/Fe] ratios were deviant compared to the other stars. If the latter two stars are included [Fe/H] = -1.30 ± 0.02.

Table 4.1 Abundances of Fe I and Fe II in NGC 288 (Spectroscopic Approach).

Star	[Fe I/H]	# of lines	[Fe II/H]	# of lines
531	-0.41	65	-0.28	4
403	-1.55	77	-1.48	12
20C	-1.44	80	-1.25	11
281	-1.31	91	-1.20	12
344	-1.33	89	-1.31	11
338	-1.40	88	-1.34	9
351	-1.36	94	-1.27	11
287	-0.71	90	-0.67	12

NGC 362

Overall average metallicity is found to be [Fe/H] = -0.94 ± 0.02. This value is obtained by not including the star MB2 which had abundances differing largely from the other stars.

Table 4.2 Abundances of Fe I and Fe II in NGC 362 (Spectroscopic Approach).

Star	[Fe I/H]	# of lines	[Fe II/H]	# of lines
1401	-0.58	68	-0.45	16
1423	-0.75	78	-0.75	13
1334	-0.90	85	-0.95	12
1441	-0.92	73	-0.86	11
1137	-0.89	84	-0.86	13
77	-1.31	83	-1.04	15
MB2	-0.54	78	-0.55	8
2127	-1.20	85	-0.75	12

Table 4.3 Average abundances for 6 stars in NGC 288 and 7 stars in NGC 362 (Spectroscopy Approach).

Elements	NGC 288	average number of lines	NGC 362	average number of lines
[Fe I/H]	-1.40 ± 0.02[a]	86.5	-0.94 ± 0.02	90.6
[Fe II/H]	-1.31 ± 0.04	11.0	-0.81 ± 0.04	13.1
[Si/Fe]	0.48 ± 0.03	8.7	0.17 ± 0.03	8.3
[Ca/Fe]	0.26 ± 0.03	14.7	-0.05 ± 0.03	15.0
[Sc II/Fe]	0.17 ± 0.07	5.8	-0.05 ± 0.05	6.0
[Ti/Fe]	0.33 ± 0.03	26.7	-0.14 ± 0.04	29.3
[Ti II/Fe]	0.38 ± 0.11	3.5	0.46 ± 0.12	2.3
[Ni/Fe]	0.10 ± 0.04	13.8	-0.12 ± 0.07	9.4
[V/Fe]	0.13 ± 0.04	10.0	-0.06 ± 0.10	10.4
[Mn/Fe]	0.12 ± 0.18	5.7	0.15 ± 0.19	5.7
[Co/Fe]	0.06 ± 0.09	6.0	-0.25 ± 0.07	6.9
[Y II/Fe]	0.40 ± 0.15	5.3	0.16 ± 0.19	5.0
[Zr/Fe]	0.52 ± 0.20	3.7	-0.23 ± 0.09	3.6
[Ba II/Fe]	0.26 ± 0.04	3.0	0.25 ± 0.06	3.0
[La IIFe]	0.56 ± 0.10	3.8	0.53 ± 0.26	3.9
[Ce II/Fe]	0.61 ± 0.12	1.3	0.12 ± 0.15	1.9
[Nd II/Fe]	0.57 ± 0.13	6.5	0.67 ± 0.22	5.9
[Eu II/Fe]	0.49 ± 0.00	1.0	0.40 ± 0.00	1.0

[a] Error in the mean was calculated assuming a normal distribution, $\sigma/\sqrt{n}$

Table 4.4 Stellar Parameters for NGC 288 (Spectroscopy Approach).

Star	$T_{\rm eff}$	$\log g$	ξ_t	[Fe/H]
531	3625	0.10	0.72	−1.30
403	4100	0.45	2.30	−1.40
20C	4100	0.80	1.97	−1.27
281	4150	0.80	1.70	−1.25
344	4225	0.90	1.78	−1.33
338	4300	1.20	1.67	−1.35
351	4315	1.20	1.71	−1.28
287	4290	1.16	0.39	−0.70

Table 4.5 Stellar Parameters for NGC 362 (Spectroscopy Approach).

Star	$T_{\rm eff}$	$\log g$	ξ_t	[Fe/H]
1401	3670	0.00	1.03	−1.20
1423	3940	0.10	1.46	−1.14
1334	3990	0.50	1.57	−1.15
1441	3900	0.40	1.78	−1.13
1137	3975	0.30	1.36	−1.15
77	4120	0.50	2.24	−1.10
MB2	3970	0.15	1.45	−1.15
2127	4060	0.75	2.03	−0.80

Table 4.6. Abundance ratios [X/Fe] for stars in NGC 288 (Spectroscopic Approach).

Star	[Si/Fe]	[Ca/Fe]	[Sc II/Fe]	[Ti/Fe]	[Ti II/Fe]	[Ni/Fe]	[V/Fe]	[Mn/Fe]	[Co/Fe]	[Y II/Fe]	[Zr/Fe]	[Ba II/Fe]	[La II/Fe]	[Ce II/Fe]	[Nd II/Fe]	[Eu II/Fe]
NGC288 531	0.14	−0.18	−0.18	−0.11	0.88	−0.02	0.19	0.06	−0.30	0.32	0.87	0.11	0.65	0.01	1.18	−0.32
NGC288 403	0.59	0.33	0.13	0.61	0.32	0.16	0.41	0.41	0.25	0.33	0.67	0.05	0.60	0.95	0.48	0.55
NGC288 20C	0.54	0.23	0.15	0.29	...	...	0.08	−0.01	0.06	0.49	0.88	0.30	0.60	0.44	0.64	0.47
NGC288 281	0.42	0.21	0.13	0.25	0.40	0.06	0.03	0.11	−0.03	0.37	0.20	0.29	0.52	0.46	0.55	0.45
NGC288 344	0.42	0.24	0.14	0.32	0.36	0.08	0.10	0.13	−0.01	0.38	0.35	0.25	0.49	0.44	0.50	0.42
NGC288 338	0.46	0.26	0.23	0.27	0.44	0.08	0.07	0.04	0.04	0.38	0.27	0.36	0.57	0.67	0.63	0.56
NGC288 351	0.45	0.26	0.22	0.23	...	...	0.10	0.05	0.05	0.42	0.72	0.30	0.56	0.69	0.62	0.49
NGC288 287	−0.04	0.03	0.26	−0.24	0.84	−0.09	−0.54	−0.24	−0.52	0.79	−0.58	0.67	0.77	−0.30	0.94	0.26

Table 4.7. Abundance ratios [X/Fe] for stars in NGC 362 (Spectroscopic Approach).

Star	[Si/Fe]	[Ca/Fe]	[Sc II/Fe]	[Ti/Fe]	[Ti II/Fe]	[Ni/Fe]	[V/Fe]	[Mn/Fe]	[Co/Fe]	[Y II/Fe]	[Zr/Fe]	[Ba II/Fe]	[La II/Fe]	[Ce II/Fe]	[Nd II/Fe]	[Eu II/Fe]
NGC362 1401	0.15	−0.17	−0.19	−0.40	0.34	−0.25	0.23	0.35	−0.34	0.19	−0.20	0.19	0.60	−0.18	0.94	0.21
NGC362 1423	−0.03	−0.10	−0.20	−0.20	0.62	−0.24	−0.26	0.00	−0.49	−0.05	−0.57	0.15	0.37	−0.28	0.41	0.17
NGC362 1334	0.05	0.01	−0.09	−0.16	...	...	0.00	0.23	−0.28	0.10	−0.27	0.26	0.48	0.03	0.63	0.39
NGC362 1441	0.19	0.02	−0.07	0.01	0.54	−0.09	0.11	0.25	−0.22	0.44	0.06	0.70	0.95	0.38	0.85	0.40
NGC362 1137	0.04	−0.01	−0.10	−0.25	...	...	−0.10	0.22	−0.34	0.05	−0.38	0.24	0.41	−0.10	0.63	0.34
NGC362 77	0.37	0.02	0.09	0.11	0.40	0.00	−0.10	0.05	−0.03	0.15	0.02	−0.05	0.42	0.51	0.52	0.58
NGC362 MB2	−0.19	−0.12	−0.14	−0.43	0.65	−0.45	−0.49	−0.26	−0.74	0.41	−0.46	0.65	0.24	−0.07	0.66	−0.02
NGC362 2127	0.43	−0.15	0.21	−0.11	0.42	0.00	−0.30	−0.02	−0.05	0.25	−0.24	0.24	0.50	0.45	0.69	0.72

4.2 Abundances from the photometric approach

NGC 288

Overall average metallicities are found to be [Fe/H] = -1.33 ± 0.02.

Table 4.8 Abundances of Fe I and Fe II in NGC 288 (Photometric Approach).

Star	[Fe I/H]	# of lines	[Fe II/H]	# of lines
531	-1.30	34	-0.86	5
403	-1.25	43	-0.88	13
20C	-1.37	38	-1.13	9
281	-1.29	53	-1.00	15
344	-1.32	53	-1.02	15
338	-1.38	59	-1.19	11
351	-1.37	60	-1.10	11
287	-1.37	69	-1.06	13

NGC 362

Overall average metallicities are found to be [Fe/H] = -1.08 ± 0.03.

Table 4.9 Abundances of Fe I and Fe II in NGC 362 (Photometric Approach).

Star	[Fe I/H]	# of lines	[Fe II/H]	# of lines
1401	-1.10	34	-0.80	8
1423	-1.02	28	-0.52	13
1334	-0.99	36	-0.68	13
1441	-1.16	26	-0.67	12
1137	-1.11	41	-0.81	11
77	-1.09	34	-0.61	11
MB2	-0.81	22	-0.61	9
2127	-1.10	38	-0.84	12

Table 4.10 Average abundances for stars in NGC 288 and NGC 362 (Photometric Approach).

Elements	NGC 288	average number of lines	NGC 362	average number of lines
[Fe I/H]	-1.33 ± 0.02[a]	51.1	-1.08 ± 0.03	33.9
[Fe II/H]	-1.03 ± 0.07	11.6	-0.69 ± 0.07	11.9
[Si/Fe]	0.51 ± 0.03	8.9	0.33 ± 0.04	8.0
[Ca/Fe]	0.17 ± 0.03	14.4	-0.05 ± 0.03	12.9
[Sc II/Fe]	0.22 ± 0.03	7.4	0.09 ± 0.04	7.7
[Ti/Fe]	0.15 ± 0.02	25.0	-0.14 ± 0.02	28.6
[Ti II/Fe]	0.54 ± 0.09	3.6	0.56 ± 0.11	3.3
[Ni/Fe]	0.07 ± 0.05	11.4	-0.10 ± 0.04	11.9
[V/Fe]	-0.01 ± 0.04	11.3	-0.19 ± 0.05	9.3
[Mn/Fe]	-0.13 ± 0.12	4.1	-0.16 ± 0.09	4.0
[Co/Fe]	0.03 ± 0.06	5.8	-0.22 ± 0.06	6.7
[Y II/Fe]	0.47 ± 0.14	5.3	0.32 ± 0.18	5.0
[Zr/Fe]	0.19 ± 0.04	2.9	-0.13 ± 0.08	3.7
[Ba II/Fe]	0.27 ± 0.00	1.0	-0.07 ± 0.06	1.8
[La/Fe]	0.57 ± 0.14	3.6	0.59 ± 0.19	3.6
[Ce II/Fe]	0.41 ± 0.16	1.6	0.34 ± 0.16	1.9
[Nd II/Fe]	0.66 ± 0.16	6.1	0.71 ± 0.16	6.0
[Eu II/Fe]	0.52 ± 0.00	1.0	0.56 ± 0.00	1.0

[a] Error in the mean was calculated assuming a normal distribution, $\sigma/\sqrt{(n)}$

Table 4.11 Stellar Parameters for NGC 288 (Photometric Approach).

Star	$T_{\rm eff}$	log g	ξ_t	[Fe I/H]
531	3811	0.386	1.75	−1.24
403	3958	0.717	1.71	−1.24
20C	4079	0.901	1.82	−1.24
281	4122	1.000	1.66	−1.24
344	4154	1.028	1.71	−1.24
338	4281	1.296	1.61	−1.24
351	4265	1.247	1.66	−1.24
287	4323	1.371	1.50	−1.24

Table 4.12 Stellar Parameters for NGC 362 (Photometric Approach).

Star	$T_{\rm eff}$	log g	ξ_t	[Fe I/H]
1401	3820	0.460	1.74	−1.16
1423	3910	0.645	1.92	−1.16
1334	3979	0.745	1.69	−1.16
1441	3889	0.613	2.10	−1.16
1137	4024	0.770	1.75	−1.16
77	3992	0.816	1.82	−1.16
MB2	4086	0.810	1.80	−1.16
2127	4075	0.853	1.74	−1.16

Table 4.13. Abundance ratios [X/Fe] for stars in NGC 288 (Photometric Approach).

Star	[Si/Fe]	[Ca/Fe]	[Sc II/Fe]	[Ti/Fe]	[Ti II/Fe]	[Ni/Fe]	[V/Fe]	[Mn/Fe]	[Co/Fe]	[Y II/Fe]	[Zr/Fe]	[Ba II/Fe]	[La II/Fe]	[Ce II/Fe]	[Nd II/Fe]	[Eu II/Fe]
NGC288 531	0.61	0.01	−0.01	0.18	0.45	0.01	−0.02	−0.20	0.06	0.41	0.33	0.05	0.33	0.49	0.80	0.44
NGC288 403	0.54	0.12	0.23	0.13	0.67	0.02	0.05	0.02	0.04	0.47	0.12	0.38	0.69	0.29	0.68	0.53
NGC288 20C	0.54	0.19	0.20	0.16	0.59	0.06	0.03	0.08	0.11	0.69	0.18	0.31	0.61	0.43	0.60	0.47
NGC288 281	0.44	0.18	0.19	0.13	0.46	0.04	−0.01	−0.18	−0.03	0.40	0.15	0.25	0.58	0.51	0.60	0.51
NGC288 344	0.48	0.18	0.24	0.13	0.48	0.11	−0.04	−0.06	−0.03	0.46	0.18	0.29	0.56	0.10	0.67	0.51
NGC288 338	0.49	0.23	0.30	0.18	0.53	0.16	0.01	−0.23	0.03	0.35	0.20	0.39	0.63	0.61	0.69	0.62
NGC288 351	0.49	0.21	0.28	0.17	0.55	0.08	−0.02	−0.21	0.04	0.52	0.17	0.29	0.60	0.73	0.66	0.54
NGC288 287	0.46	0.22	0.31	0.15	0.58	0.10	−0.08	−0.22	−0.01	0.48	0.15	0.23	0.59	0.09	0.61	0.54

Table 4.14. Abundance ratios [X/Fe] for stars in NGC 362 (Photometric Approach).

Star	[Si/Fe]	[Ca/Fe]	[Sc II/Fe]	[Ti/Fe]	[Ti II/Fe]	[Ni/Fe]	[V/Fe]	[Mn/Fe]	[Co/Fe]	[Y II/Fe]	[Zr/Fe]	[Ba II/Fe]	[La II/Fe]	[Ce II/Fe]	[Nd II/Fe]	[Eu II/Fe]
NGC362 1401	0.34	−0.05	0.00	−0.02	0.59	−0.03	0.08	0.10	−0.51	0.48	0.32	...	0.56	0.30	0.87	0.58
NGC362 1423	0.33	−0.21	0.03	−0.29	0.53	−0.16	−0.42	−0.27	−0.23	0.14	−0.42	−0.60	0.48	0.11	0.48	0.53
NGC362 1334	0.25	0.01	0.11	-0.10	0.58	−0.12	−0.12	−0.03	−0.17	0.23	−0.23	0.26	0.57	0.20	0.52	0.57
NGC362 1441	0.49	0.06	0.11	0.04	0.58	0.06	0.00	0.00	−0.01	0.56	0.15	−0.35	1.10	0.80	1.09	0.65
NGC362 1137	0.27	0.04	0.09	−0.03	0.40	−0.07	−0.08	−0.08	−0.11	0.20	−0.09	0.14	0.51	0.23	0.71	0.62
NGC362 77	0.33	−0.14	0.18	−0.35	0.65	−0.09	−0.46	−0.31	−0.19	0.21	−0.48	−0.07	0.46	0.44	0.43	0.58
NGC362 MB2	0.13	−0.06	0.12	−0.20	0.52	−0.29	−0.26	−0.45	−0.37	0.56	0.02	...	0.54	0.31	0.89	0.38
NGC362 2127	0.30	−0.04	0.13	−0.18	0.47	−0.09	−0.25	−0.24	−0.16	0.19	−0.27	0.21	0.48	0.29	0.66	0.58

4.3 Abundance dependencies on model parameters

The estimated internal errors are $T_{\rm eff}+50$ K, $\log(g)=0.3$, [m/H] + 0.2 and $\xi_t+0.2$. The variance in the abundance (not including the cross terms, as their effect is small) was adopted from Johnson (2002). The estimated internal errors were calculated as the sum of the first four terms added in quadrature:

$$\sigma^2_{\log\epsilon} = \sigma^2_{T_{\rm eff}} + \sigma^2_{\log(g)} + \sigma^2_{\rm [m/H]} + \sigma^2_{\xi_t} \tag{4.1}$$

The internal errors where estimated by varying one parameter at the time and noting the difference in abundance. Below is a table showing the abundance dependencies on model parameters using NGC 288-344 as an example.

Table 4.15 Abundance dependencies on model[a] parameters.

Element Abundance	$T_{\rm eff}+50$ K	$\log(g)+0.3$	[m/H] + 0.2	$\xi_t+0.2$	Total ($\log\epsilon$)
Δ[Fe I/H]	−0.05	−0.01	0.00	0.13	0.14
Δ[Fe II/H]	0.05	−0.16	0.07	0.05	0.19
Δ[Si/Fe]	0.06	−0.05	0.02	0.01	0.08
Δ[Ca/Fe]	−0.03	0.03	−0.04	0.10	0.12
Δ[Sc II/Fe]	0.06	−0.11	0.06	0.07	0.16
Δ[Ti/Fe]	−0.05	0.02	−0.04	0.05	0.08
Δ[Ti II/Fe]	0.05	−0.11	0.05	0.12	0.18
Δ[Ni/Fe]	0.02	−0.04	0.02	0.05	0.07
Δ[V/Fe]	−0.06	0.01	−0.04	0.06	0.09
Δ[Mn/Fe]	−0.03	0.00	−0.02	0.10	0.11
Δ[Co/Fe]	0.00	−0.03	0.00	0.01	0.03
Δ[Y II/Fe]	0.05	−0.10	0.06	0.08	0.15
Δ[Zr/Fe]	−0.08	0.00	−0.04	0.01	0.09
Δ[Ba II/Fe]	0.03	−0.09	0.07	0.19	0.22
Δ[La/Fe]	0.04	−0.10	0.01	0.09	0.14
Δ[Ce II/Fe]	0.04	−0.11	0.06	0.02	0.13
Δ[Nd II/Fe]	0.03	−0.11	0.05	0.07	0.14
Δ[Eu II/Fe]	0.05	−0.12	0.07	0.02	0.15

[a] NGC 288-344: $T_{\rm eff}$= 4225 K, $\log g = 0.90$ cm s^{-2}, $\xi_t = 2.10$ km s^{-1}.

4.4 Predicted and observed scatter in abundance ratios

Using the results from the previous section by defining $\sigma^2_{\log \epsilon} = \sigma_{\text{predicted}}$, one can show that the abundance deviations can in most cases be explained entirely by measurement uncertainties.

Table 4.16 Comparison of predicted and observed spread in abundances in NGC 288 (Spectroscopic Approach).

[X/Fe]	$\sigma_{\text{predicted}}$	σ_{observed}
[Fe I/H]	0.14	0.17
[Fe II/H]	0.19	0.15
[Si/Fe]	0.08	0.08
[Ca/Fe]	0.12	0.09
[Sc II/Fe]	0.16	0.12
[Ti/Fe]	0.08	0.16
[Ti II/Fe]	0.18	0.19
[Ni/Fe]	0.07	0.16
[V/Fe]	0.09	0.16
[Mn/Fe]	0.11	0.18
[Co/Fe]	0.03	0.22
[Y II/Fe]	0.15	0.34
[Zr/Fe]	0.09	0.39
[Ba II/Fe]	0.22	0.08
[La/Fe]	0.14	0.20
[Ce II/Fe]	0.13	0.16
[Nd II/Fe]	0.14	0.33
[Eu II/Fe]	0.15	...

Note. — Star NGC288-531 and NGC288-287 have been omitted due to their deviating [Fe/H]. In most cases $\sigma_{\text{predicted}} < \sigma_{\text{observed}}$, which shows that the abundance deviations in most cases can be explained entirely by measurement uncertainties. Only one Eu II line was measured, thus no σ_{observed} value.

4.5 Result Comparison

Below follows a result comparison between the clusters, the two approaches and another results in literature.

4.5.1 Comparison between the clusters

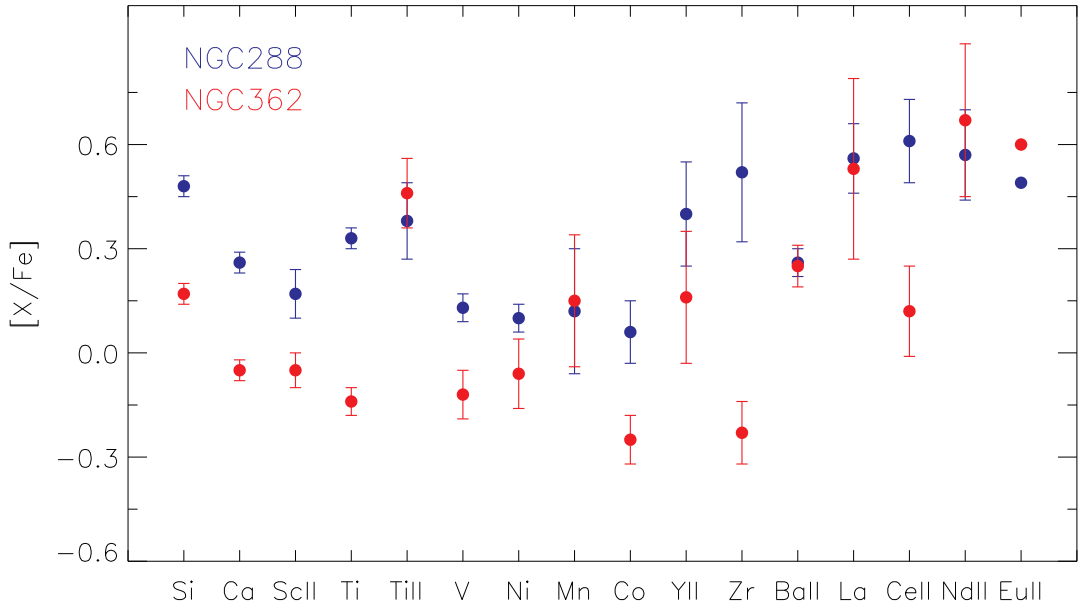

Figure 4.1 Average [X/Fe] for 6 stars (not including 531 and 287) in NGC 288 and 7 stars (not including MB2) in NGC 362 (Spectroscopy Approach).

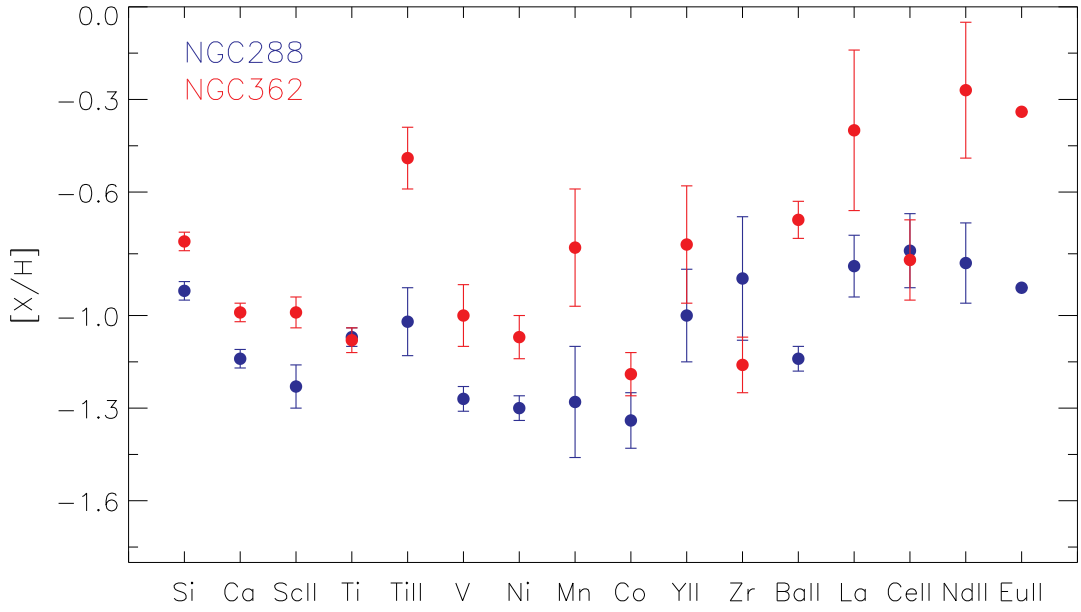

Figure 4.2 Average [X/H] for 6 stars (not including 531 and 287) in NGC 288 and 7 stars (not including MB2) in NGC 362 (Spectroscopy Approach).

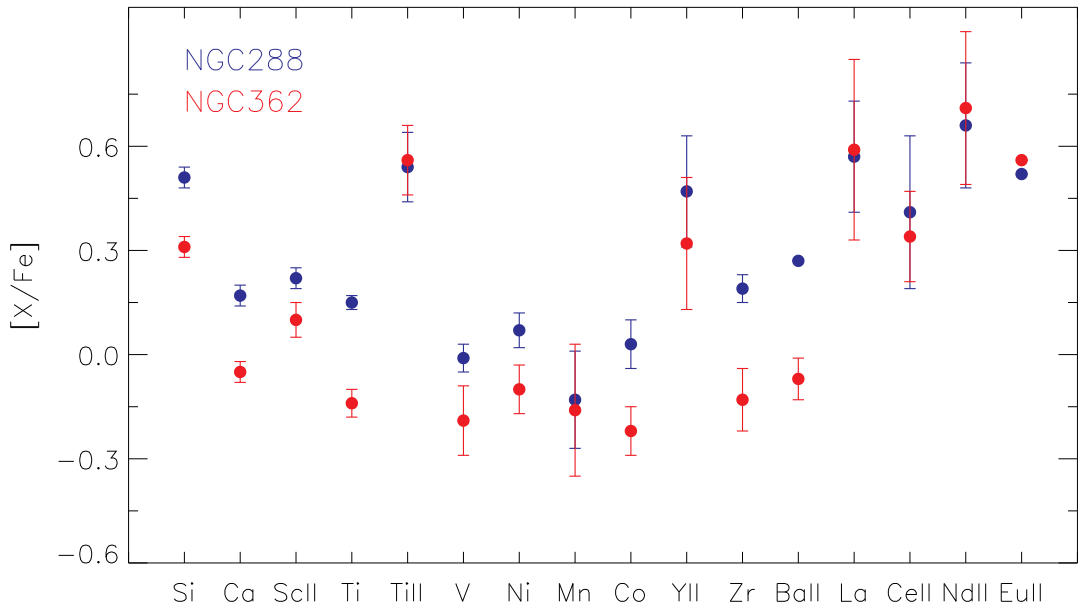

Figure 4.3 Average [X/Fe] for 8 stars in NGC 288 and 8 stars in NGC 362 (Photometric Approach).

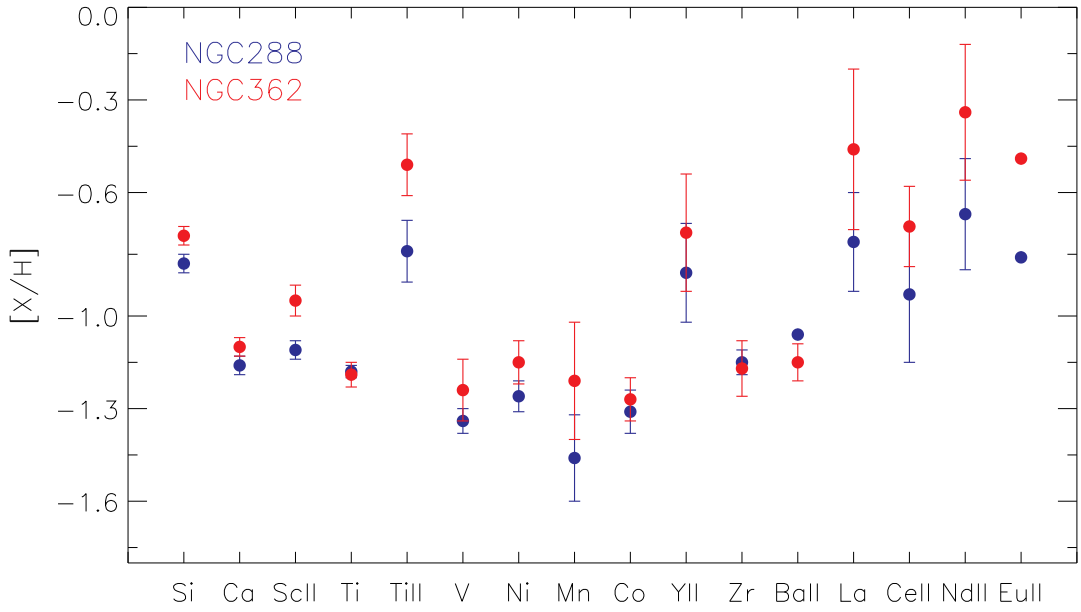

Figure 4.4 Average [X/H] for 8 stars in NGC 288 and 8 stars in NGC 362 (Photometric Approach).

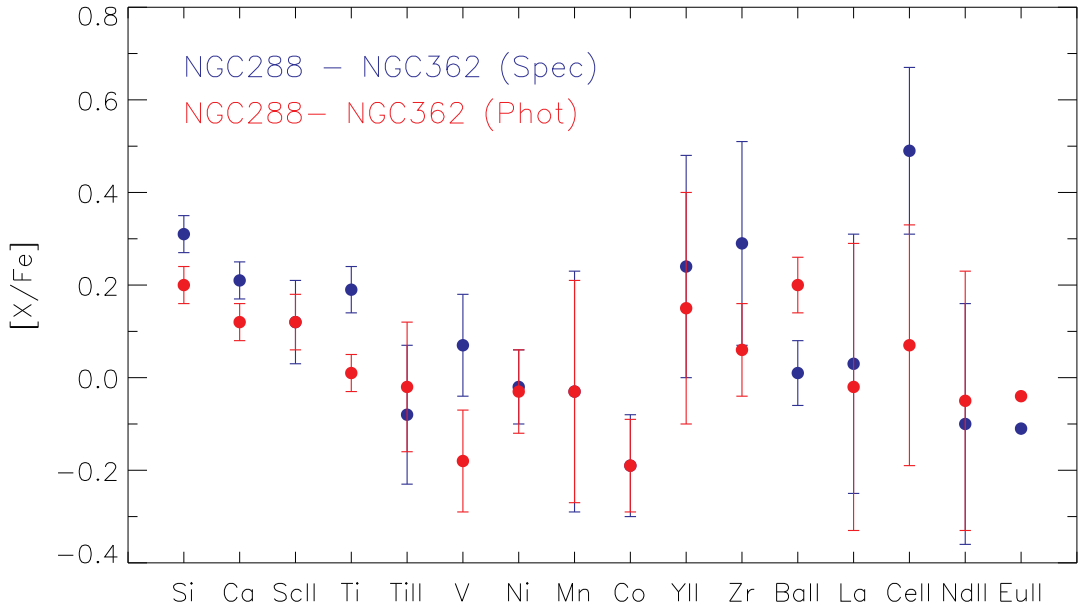

Figure 4.5 Average [X/Fe] difference between the clusters.

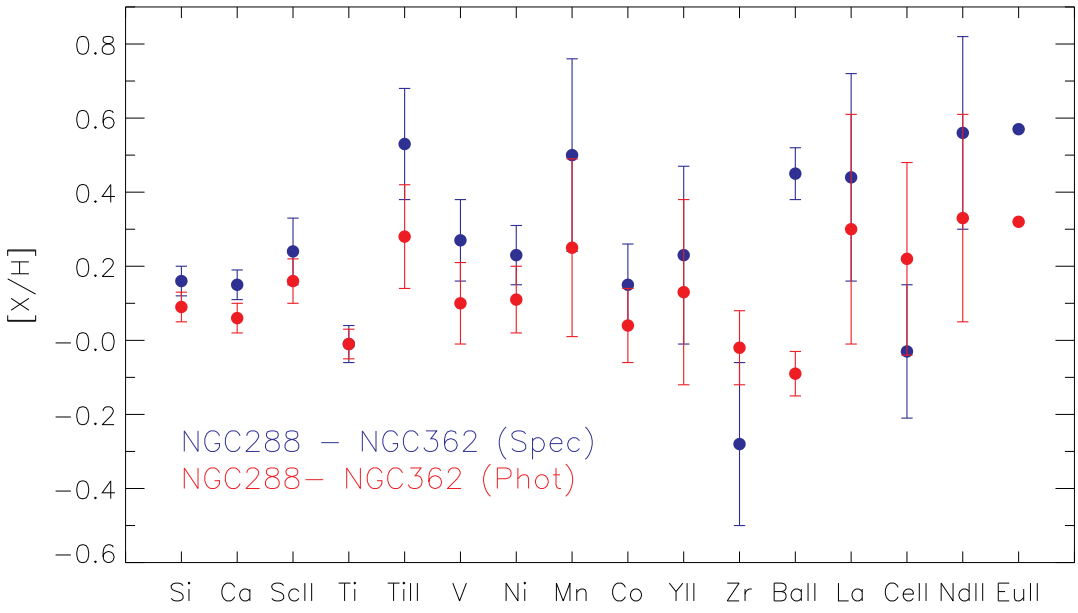

Figure 4.6 Average [X/H] difference between the clusters.

4.5.2 Comparison between the spectroscopic and photometric approach

Below the two approaches are compared for both NGC 288 and NGC 362.

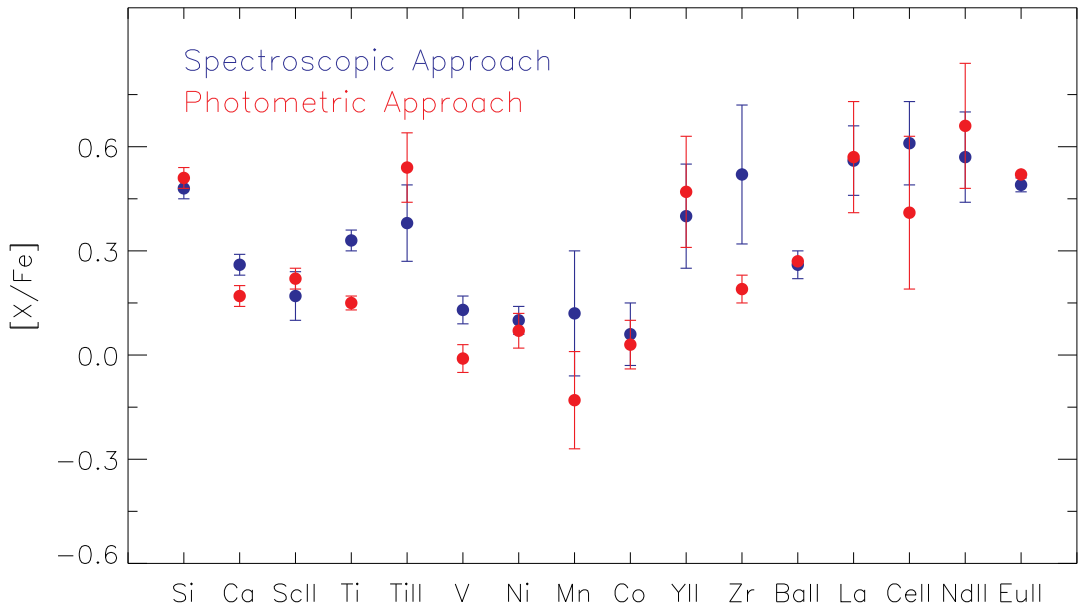

Figure 4.7 Average abundance of stars in NGC 288 derived using a spectroscopic approach (blue) and a photometric approach (red).

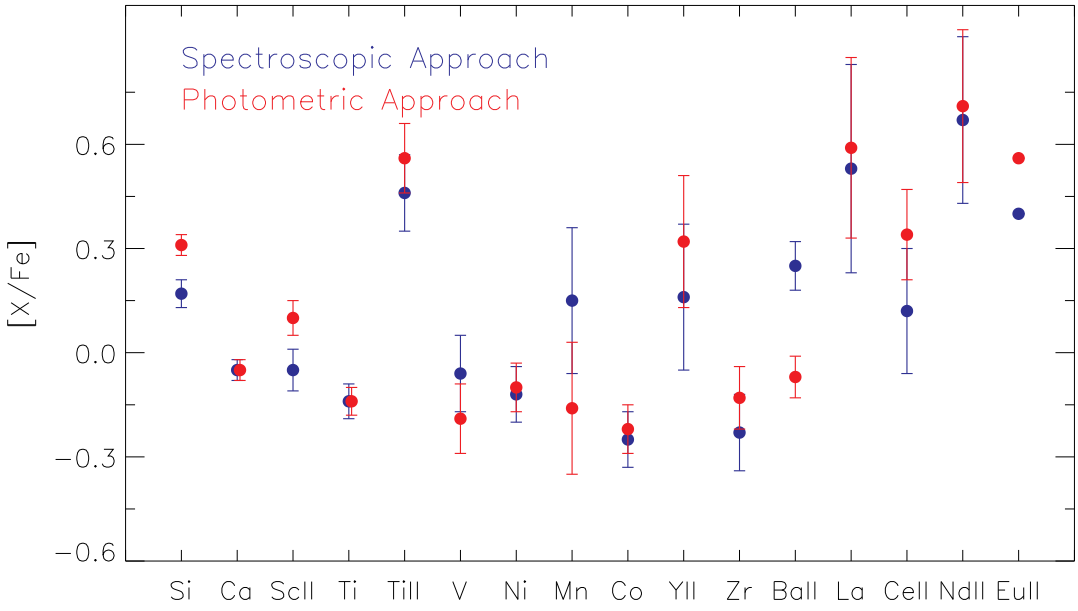

Figure 4.8 Average abundance of stars in NGC 362 derived using a spectroscopic approach (blue) and a photometric approach (red).

4.5.3 Comparison with other results in literature

Table 4.17 Parameters $T_{\rm eff}$ and $\log g$ for NGC 288 compared with Shetrone & Keane (2000).

Star	$T_{\rm eff}{}_{spec}$	$T_{\rm eff}{}_{phot}$	$T_{\rm eff}{}_{\rm SK}$	$\log g$ $_{spec}$	$\log g$ $_{phot}$	$\log g$ $_{\rm SK}$
531	3625	3811	3780	0.10	0.386	0.10
403	4100	3958	3950	0.45	0.717	0.20
20C	4100	4079	4050	0.80	0.901	0.60
281	4150	4122	4125	0.80	1.000	0.60
344	4225	4154	4180	0.90	1.028	0.80
338	4300	4281	4325	1.20	1.296	1.30
351	4315	4265	4330	1.20	1.247	1.20
287	4290	4323	4350	1.16	1.371	1.20
Average	**4198**	**4124**	**4136**	**0.89**	**0.99**	**0.75**

Table 4.18 Parameters ξ_t and [Fe/H] for NGC 288 compared with Shetrone & Keane (2000).

Star	ξ_t $_{spec}$	ξ_t $_{phot}$	ξ_t $_{\rm SK}$	[Fe/H] $_{spec}$	[Fe/H] $_{phot}$	[Fe/H] $_{\rm SK}$
531	0.72	1.75	1.60	−1.30	−1.24	−1.31
403	2.30	1.71	1.90	−1.40	−1.24	−1.43
20C	1.97	1.82	1.75	−1.27	−1.24	−1.44
281	1.70	1.66	1.71	−1.25	−1.24	−1.42
344	1.78	1.71	1.60	−1.33	−1.24	−1.36
338	1.67	1.61	1.60	−1.35	−1.24	−1.37
351	1.66	1.71	1.55	−1.28	−1.24	−1.33
287	1.50	0.39	1.40	−0.70	−1.24	−1.45
Average	**1.85**	**1.55**	**1.64**	**−1.31**	**−1.24**	**−1.39**

Table 4.19 Parameters $T_{\rm eff}$and $\log g$ for NGC 362 compared with Shetrone & Keane (2000).

Star	$T_{\rm eff}{}_{spec}$	$T_{\rm eff}{}_{phot}$	$T_{\rm eff}{}_{\rm SK}$	$\log g$ $_{spec}$	$\log g$ $_{phot}$	$\log g$ $_{\rm SK}$
1401	3670	3820	3875	0.00	0.460	0.00
1423	3940	3910	3950	0.10	0.645	0.10
1334	3990	3979	3975	0.50	0.745	0.40
1441	3900	3889	3975	0.40	0.613	0.20
1137	3975	4024	4000	0.30	0.770	0.70
77	4120	3992	4075	1.50	0.816	0.20
MB2	3970	4086	4100	0.15	0.810	0.60
2127	4060	4075	4110	0.75	0.853	0.60
Average	**3933**	**3957**	**3993**	**0.47**	**0.69**	**0.31**

cd

Table 4.20 Parameters ξ_t and [Fe/H] for NGC 362 compared with Shetrone & Keane (2000).

Star	$\xi_{t\ spec}$	$\xi_{t\ phot}$	$\xi_{t\ \mathrm{SK}}$	[Fe/H] $_{spec}$	[Fe/H] $_{phot}$	[Fe/H] $_{\mathrm{SK}}$
1401	1.03	1.74	1.90	−1.20	−1.16	−1.32
1423	1.46	1.92	2.35	−1.14	−1.16	−1.37
1334	1.57	1.69	1.95	−1.15	−1.16	−1.30
1441	1.78	2.10	1.90	−1.13	−1.16	−1.31
1137	1.36	1.75	2.00	−1.15	−1.16	−1.37
77	2.24	1.82	2.50	−1.10	−1.16	−1.34
MB2	1.45	1.80	2.50	−1.15	−1.16	−1.33
2127	2.03	1.74	2.25	−0.80	−1.16	−1.30
Average	**1.64**	**1.82**	**2.17**	**−1.10**	**−1.16**	**−1.33**

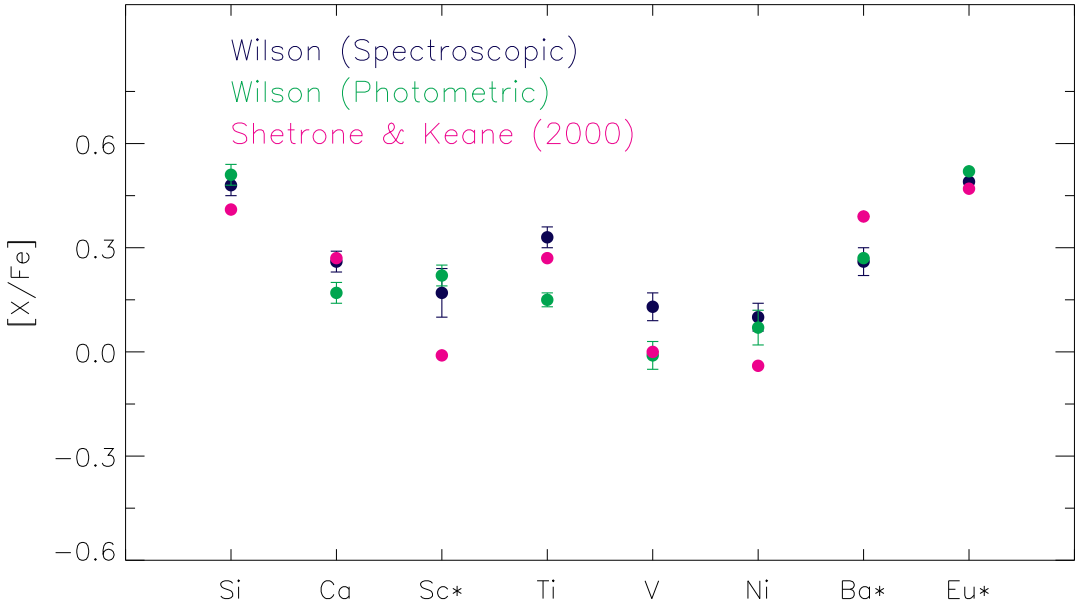

Figure 4.9 Result comparison for NGC 288 with Shetrone & Keane (2000). The * after the chemical symbol indicates that [X I/Fe] is being compared to [X I/Fe] where X is the chemical element. This is done as the analysis assumes [X I/Fe] = [X II/Fe].

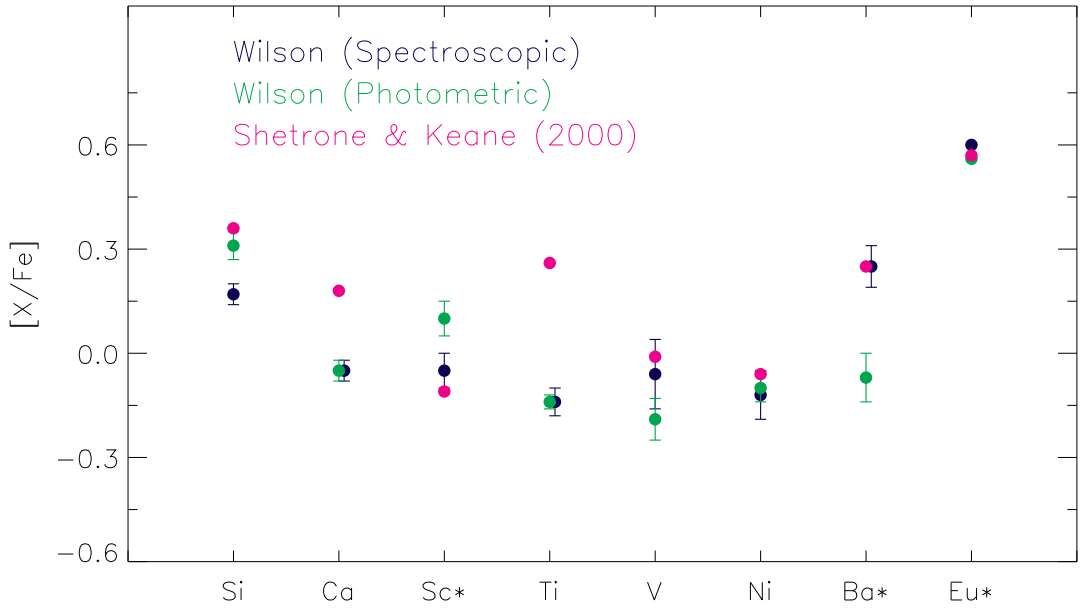

Figure 4.10 Result comparison for NGC 362 with Shetrone & Keane (2000). The * after the chemical symbol indicates that [X I/Fe] is being compared to [X I/Fe] where X is the chemical element. This is done as the analysis assumes [X I/Fe] = [X II/Fe].

5 DISCUSSION

5.1 Abundances

Below follows a discussion of the elemental abundances.

5.1.1 [Fe I/H] and [Fe II/H]

Spectroscopic Approach

In NGC 288 the overall average metallicity is found to be [Fe/H] = -1.40 ± 0.02 using the spectroscopic approach. This value is obtained by not including the stars 531 and 287. The reason for not including these stars is due to their deviating [Fe I/H] values compared to the other stars (see table 4.1). If the latter two stars are included [Fe/H] = -1.30 ± 0.02. Although this value seems to be closer to that of Harris (1996) which refers to a value of [Fe/H] = -1.24, this is only the case as the two omitted stars with both lower [Fe/H] throw of the mean. The results from the analysis show that NGC 288 has a 0.16 dex lower [Fe/H] compared to Harris (1996) using the spectroscopic approach.

In NGC 362 the overall average metallicities are found to be [Fe/H] = -0.94 ± 0.02 using the spectroscopic approach. This value is obtained by not including the star MB2. MB2 had a [X/Fe] values very different from the other stars. As seen in table 4.1, [Si/Fe], [Mn/Fe] and [Eu II/Fe] all have abundance varying greatly compared to the other stars. Harris (1996) refers to a value of [Fe/H] = -1.16 for the cluster. The results from the analysis show that NGC 362 has a 0.22 dex higher [Fe/H] as compared to Harris (1996) using the spectroscopic approach.

Photometric Approach

In NGC 288 the overall average metallicity is found to be [Fe/H] = -1.33 ± 0.02 using the photometric approach. The results from the analysis show that NGC 288 has a 0.09 dex lower [Fe/H] compared to Harris (1996) using the photometric approach. All the stars in 288 where included as their [Fe I/H] and [X/Fe] were consistent.

In NGC 362 the overall average metallicities are found to be [Fe/H] = -1.08 ± 0.03 using the photometric approach. The results from the analysis show that NGC 362 has a 0.14 dex higher [Fe/H] as compared to Harris (1996) using the photometric approach. All the stars in 362 where included as their [Fe I/H] and [X/Fe] were consistent.

The [Fe I/H] and [Fe II/H] differ quite a bit as seen in table 4.8. This is because the model parameters once found were not changed as they were in the spectroscopic approach. To further make sure that most of the EWs were measured on the linear part of the curve of growth lines with a EW greater than 150mÅ were not included[1]. This lead to fewer Fe I lines being included as seen in tables 4.8 and 4.9 compared to tables 4.1 and 4.2.

5.1.2 α Elements

The α elements are those light elements with atomic numbers $Z \leq 22$ whose most abundant isotopes are multiples of ^{4}He nuclei. The α elements are as follows: C, O, Ne, Mg, Si, S, Ar, Ca and Ti. The elemets included in this study are: Si, Ca and Ti. Ti is regarded as an "honourary" α element since observers find it to act like the other α elements though theorists believe it should scale with Fe. Observations show [Ti/Fe] $\sim$ 0.3 dex in the halo whereas theorists predict [Ti/Fe] = 0 (Timmes et al. 1995). Carbon is an element that was not studied as it shows large star-to-star abundance variations in all globular clusters. Also this element can be synthesised and destroyed by nuclear burning even in cores of low-mass stars (Gratton et al. 2004).

Large amounts of α elements relative to Fe, are produced in Type Ib/c and II supernovae, so called core-collapse supernovae (CCSNe), which are the end result of short lived, massive stars. Type Ia supernovae (SNe Ia), which have longer lifetimes of $\sim$ 1 Gyr, produce no α elements, but instead Fe and Fe-peak elements. Thus, when low metallicity stars were being born, only CCSNe had contributed to the Galactic chemical evolution, explaining their high [α/Fe] ratios. Once SNe Ias started to contribute, after $\sim$ 1 Gyr, more Fe would have been produced lowering the [α/Fe] ratio from a halo-like value of about 0.3 dex at [Fe/H]= -1 to about [α/Fe]= 0 at [Fe/H]= 0. If the star formation rate had been high, the CCSNe would have caused higher α abundances relative to Fe, before the SNe Ia would have started to contribute. Examples of this are the bulge and thick disk where [α/Fe] exceeds the value of the stars located in the thin disk. If, on the other hand, the star formation had been slow, fewer α elements would be created through CCSNe, causing the [α/Fe] to drop as the SNe Ia would start to contribute. Examples of this are the dwarf spheroidal galaxies where the [α/Fe] ratios are much lower than for stars in the halo.

[1]The decision to do this came from the spectroscopic approach which was done first. The spectroscopic results showed that measuring lines greater than 150mÅ lead to a greater spread in [Fe I/H]. This was due to abundances being calculated using the flat region on the curve of growth where a slight change in EWs causes large changes in abundances. See section 5.3.2

[α/**Fe**]

The results show a consistent over abundance of α elements in NGC 288 as compared to NGC 362 as seen in tables 4.3, 4.10 and figures 4.1, 4.3. The average difference in α abundances for the two clusters are $\langle\Delta[\alpha/\mathrm{Fe}]^{\mathrm{spec}}_{NGC|288-362|}\rangle = 0.25$ dex ($\sigma = 0.03$) and $\langle\Delta[\alpha/\mathrm{Fe}]^{\mathrm{phot}}_{|NGC288-362|}\rangle = 0.11$ dex. Compared to other studies such as that of Gratton (1987) and Shetrone & Keane (2000) the difference between the clusters should be within 0.1 dex. Shetrone & Keane (2000) for instance have that $\Delta[\alpha/\mathrm{Fe}]_{|NGC288-362|} = 0.05$ dex. Thus this study shows a much larger difference in α element abundances between the clusters. Most likely this is due to the abundance analysis of stars in NGC 362 where an incorrect determination of the [Fe/H] values might have occurred. This occurrence would effect the abundace elements as their [X/Fe] are all dependant on [Fe/H]. In figures 4.2 and 4.4 were this dependancy on Fe has been removed, the difference in α element abundances are much smaller. Why the [Fe/H] might have been determined incorrectly in this cluster is not yet know. The suspicion arises from the varying [Fe/H] seen in table 4.2 and how the [Fe/H] values don't match very well with the [Fe/H] values from Shetrone & Keane (2000) seen in table 4.20.

Compared to Shetrone & Keane (2000) the abundances of Si and Ca match very well (within ~ 0.1 dex) apart from the abundance of Ca in NGC 362 which is off by 0.23 dex. The enhanced abundance of Si is accompanied by a similar excess in both the two other α elements Ca and Ti. Shetrone & Keane (2000) confirms this result (see figure 4.9). The production of Si and Ca are produced when incomplete explosive Si burning and explosive O burning takes place in massive stars. Thus it is natural that Si should be accompanied by a similar excess of Ca. This is a classic signature of α-elements in metal-poor stars (Wheeler et al. 1989).

[α/**H**]

By looking at the abundances relative to hydrogen, any bias in [Fe/H] is removed. The average difference in α abundances was reduced by removing this bias. The average abundance differences are $\langle\Delta[\alpha/\mathrm{H}]^{\mathrm{spec}}_{|NGC288-362|}\rangle = 0.11$ dex ($\sigma = 0.08$) and $\langle\Delta[\alpha/\mathrm{H}]^{\mathrm{phot}}_{|NGC288-362|}\rangle = 0.10$ dex ($\sigma = 0.05$), the last one of which is the same as Shetrone & Keane (2000). Figure 4.6 shows a decrease in the average [α/H] differences as compared to the average [α/H] differences shown in figure 4.5.

5.1.3 Fe-peak elements

The Fe-peak elements in this abundance analysis are Sc, V, Ni, Mn and Co.

[X/Fe]

Much like the abundances of the α elements the Fe-peak show a consistent over abundance in NGC 288 as compared to NGC 362 as seen in tables 4.3, 4.10 and figures 4.1, 4.3. The abundance difference is smaller though than the α elements in both clusters. The Mn abundances are very similar for both clusters and differ only by 0.02 dex. The Co abundance difference is very constant between the clusters. Co also changes very little depending on the approach used. The stability of the Co abundance is seen in table 4.15 where it has the smallest abundance dependence on the model parameters.

The abundance of the Fe-peak elements Sc II, Ni and V compare reasonably well to the results form Shetrone & Keane (2000) yet not as well as NGC 362 as seen in figures 4.9 and 4.10. For NGC 288 $\langle\Delta[(\mathrm{Scii,V,Ni})/\mathrm{Fe}]^{\mathrm{spec}}_{|288-\mathrm{SK}|}\rangle = 0.15$ dex ($\sigma = 0.03$) and $\langle\Delta[(\mathrm{Scii,V,Ni})/\mathrm{Fe}]^{\mathrm{phot}}_{|288-\mathrm{SK}|}\rangle = 0.12$ dex ($\sigma = 0.11$). For NGC 362 $\langle\Delta[(\mathrm{Scii,V,Ni})/\mathrm{Fe}]^{\mathrm{spec}}_{|362-\mathrm{SK}|}\rangle = 0.05$ dex ($\sigma = 0.01$) and $\langle\Delta[(\mathrm{Scii,V,Ni})/\mathrm{Fe}]^{\mathrm{phot}}_{|362-\mathrm{SK}|}\rangle = 0.14$ dex ($\sigma = 0.09$).

[X/H]

The average abundance differences between the clusters for the Fe-peak elements are: $\langle\Delta[(\mathrm{Scii,V,Ni})/\mathrm{X}]^{\mathrm{spec}}_{|NGC288-362|}\rangle = 0.25$ dex ($\sigma = 0.02$) and $\langle\Delta[(\mathrm{Scii,V,Ni})/\mathrm{X}]^{\mathrm{phot}}_{|NGC288-362|}\rangle = 0.12$ ($\sigma = 0.03$).

5.1.4 Neutron-Capture Elements

Through stellar nucleosynthesis the number of protons in the atom (Z) increases. As the atoms get larger their Coulomb barrier increases and it becomes more difficult for other charged particles such as protons and alpha particles protons to react with them. This is however, not the case when neutrally charged neutrons collide with the atom. The neutrons don't have a Coulomb barrier they have to tunnel through and thus the neutrons are not as dependant on temperature. With enough energy and neutrons, nuclear reactions will occur. In this GC abundance analysis, like most other studies, the brightest cluster members have been observed. These stars are cool giants with a black body spectrum peaking towards the longer wavelengths having low fluxes towards the shorter wavelengths. Neutron-capture (N-capture) elements which arise from their ionised species however, have most of the strong transition lines at wavelengths below 5000 Å. Thus the number of n-capture abundances derived from GC is quite small. The neutron capture elements all have an atomic number $Z > 30$. These elements can further be divided into the s-process, r-process and p-process elements.

5.1.5 The s-process elements

If the beta-decay half-life is short compared to the time scale for neutron capture, the neutron capture reaction is said to be a *slow process* or an **s-process** reaction (Carroll & Ostlie 2007). If the neutron flux is low the absorbed neutrons have time to decay into other nuclei before new neutrons are captured (Burbidge et al. 1957). The s-process typically occurs during helium burning in the cores of low to intermediate mass stars. It is mainly responsible for Solar System abundances of elements such as Sr, Zr, Ba and La (Gratton et al. 2004). In this study the abundances of s-process elements Y, Zr, Ba, La and Ce are presented.

[X/Fe]

All the s-process elements have greater abundance ratios [X/Fe] in NGC 288 relative to NGC 362 apart from [Fe/La] from the photometric approach. These 5 s-process elements have an average abundance of $\langle \Delta[X/\mathrm{Fe}]^{\mathrm{spec}}_{|NGC288-362|} \rangle = 0.21$ dex ($\sigma = 0.20$) and $\langle \Delta[X/\mathrm{Fe}]^{\mathrm{phot}}_{|NGC288-362|} \rangle = 0.09$ dex ($\sigma = 0.09$). The standard deviation between these elements are rather large. The main reason for this is the hyperfine structure splitting and/or isotopic splitting which have neither been taken into account in this analysis. Ba for example is affected by isotopic splitting whilst La is affected by hyperfine structure splitting. There are well established methods that account for these effects, but these have not yet been included in the present analysis, but will be included at a later stage. The only s-process element which can be compared to Shetrone & Keane (2000) is Ba. Both approaches give similar [Ba II/Fe] which have a 0.12 dex lower abundances compared to [Ba/Fe] from Shetrone & Keane (2000).

The only s-process element which is not as affected by this is Ce. Nd which is about about 50% r-process and 50% s-process (Burris et al. 2000) is also not as affected.

[X/H]

The average abundance differences between the clusters for the s-process elements are: $\langle \Delta[X/\mathrm{H}]^{\mathrm{spec}}_{|NGC288-362|} \rangle = 0.16$ dex ($\sigma = 0.32$) and $\langle \Delta[X/\mathrm{H}]^{\mathrm{phot}}_{|NGC288-362|} \rangle = 0.11$ dex ($\sigma = 0.16$).

5.1.6 The r-process elements

If the half-life for the beta-decay reaction is long compared with the time scale for neutron capture, the neutron-capture reaction is said to be a *rapid process* or **r-process** and results in neutron-rich nuclei (Carroll & Ostlie 2007). R-process elements are created in events such as deaths of high mass stars. The r-process is mainly responsible for the Solar System abundances of, for example, Rh, Ag, Eu

and Pt (Gratton et al. 2004). The only r-process element present in this study is Eu found at 6645 Å.

[Eu II/Fe]

The results from both spectroscopic and photometric approach would suggest that NGC 362 formed from material with a higher concentration of r-process products than NGC 288. Apart from the abundance of La in the photometric approach, the 4 other s-process elements (Y II, Zr, Ba II and Ce II) all show a consistently lower abundance in NGC 362 both using the spectroscopic and photometric approaches. The higher [Eu II/Fe] and lower s-process abundance for NGC 362 relative to NGC 288 indicate that the NGC 362 stars formed from gas that was enriched in r-process products but deficient in s-process products relative to the mixtures in the gas that formed the NGC 288 stars.

From the spectroscopic approach the difference in [Eu II/Fe] between the clusters was found to be 0.11 dex and for the photometric approach 0.04 dex. Due to there only being one Eu II line in all the spectra it is not possible to calculate the errors. The result is consistent with Shetrone & Keane (2000) who found an average difference of 0.08 dex, where NGC 362 has a greater [Eu II/Fe]. Future studies could confirm this result by doing an abundance analysis of Th, which is a radioactive pure r-process element which should show a similar trend to Eu.

[Eu II/H]

Unlike the α elements, removing the dependence on [Fe/H] the difference between the Eu II abundances are much larger. Still the abundance of Eu II is larger in NGC 362. Thus using the [Fe/H] or not, the same result remain the same as the above subsection.

5.1.7 The p-process elements

A third process for heavy element formation is the p-process. This process produces some of the isotopes heavier than Fe that cannot be built by either the s or the r-process on any time scale (Burbidge et al. 1957). This abundance analysis did not cover any p-process elements.

5.2 Comparison of the spectroscopic and photometric approach

The two separate approaches in creating the stellar models lead to two sets of abundances for each star in each cluster. Each approach have their weaknesses and strengths. The spectroscopic approach is more affected by departures from LTE, which causes an incorrect estimation of [Fe II/H]. Apart from the assumption of LTE, the spectroscopic approach does not assume any stellar parameters such as mass or colour temperature.

The photometric approach has errors when determining the physical gravity due to inaccuracies in distance measurements from parallax measurements. Also affecting the physical gravity is the the stellar mass, which was assumed in determining $\log(g)$. Errors were also introduced when estimating a temperature as the colour temperature relations are model dependent. That is, a specific set of models were used.

5.2.1 The preferred approach

To evaluate which approach is preferred, two scenarios are adopted. In the first scenario, it is assumed that the Shetrone & Keane (2000) abundances are correct and that the preferred approach should reproduce most accurately those results. In this scenario, the spectroscopic approach produces abundances that more closely match Shetrone & Keane (2000) than does the photometric approach. This result holds for both clusters. $\langle \Delta[X/\mathrm{Fe}]^{288\ \mathrm{spec}}_{|\mathrm{Wilson-SK}|} \rangle = 0.09$ dex ($\sigma = 0.06$) compared to $\langle \Delta[X/\mathrm{Fe}]^{288\ \mathrm{phot}}_{|\mathrm{Wilson-SK}|} \rangle = 0.11$ dex ($\sigma = 0.06$) and $\langle \Delta[X/\mathrm{Fe}]^{362\ \mathrm{spec}}_{|\mathrm{Wilson-SK}|} \rangle = 0.13$ dex ($\sigma = 0.14$) compared to $\langle \Delta[X/\mathrm{Fe}]^{362\ \mathrm{phot}}_{|\mathrm{Wilson-SK}|} \rangle = 0.18$ dex ($\sigma = 0.14$).

In the second scenario, it is assumed that the clusters are chemically homogeneous and therefore the preferred approach is the one which produces the lowest observed dispersion. In this scenario, the preferred approach is the photometric approach which produces the lowest dispersion. $\langle \Delta[X/\mathrm{Fe}]^{\mathrm{spec}}_{|288-362|} \rangle = 0.16$ dex ($\sigma = 0.13$) compared to $\langle \Delta[X/\mathrm{Fe}]^{\mathrm{phot}}_{|288-362|} \rangle = 0.09$ dex ($\sigma = 0.07$). Even if one compares [X/H] the same result is found $\langle \Delta[X/\mathrm{H}]^{\mathrm{spec}}_{|288-362|} \rangle = 0.30$ dex ($\sigma = 0.18$) and $\langle \Delta[X/\mathrm{H}]^{\mathrm{phot}}_{|288-362|} \rangle = 0.16$ dex ($\sigma = 0.11$).

Thus, if one assumes that the Shetrone & Keane (2000) abundances are correct the spectroscopic approach is preferred, whereas if one assumes that the clusters are chemically homogeneous the photometric approach is preferred.

5.2.2 Constraints on the abundance differences between the clusters.

The current [X/Fe] measurements serve as upper limits on the element abundances in the two clusters. This is because hyperfine and/or isotopic splitting was not taken into account. If these effects had been taken into account, the inferred abundances would be lower. The weak lines would not be affected much by these effects, however, in cases where the lines are strong, the revised abundance would be lower since line splitting has the effect of delaying the onset of saturation.

5.3 Errors

All the abundance measurements were assumed to have the same error. Since their equivalent measurement technique was the same, a normal distribution was assumed. With this the error in the mean was calculated by dividing the standard deviation by $\sqrt{n}$. Comparing the predicted and observed scatter in the abundance ratios (table 4.16) it is seen that $\sigma_{\text{predicted}} < \sigma_{\text{observed}}$ for the most cases. This shows that the deviations can be explained entirely by measurement uncertainties. There are a number of different sources of error in this abundance analysis. Below some of the most likely sources of the errors are presented.

5.3.1 Model atmospheres

Model atmospheres play an important part in an abundance analysis, thus it was worth studying to what extent the a different model would influence the abundances. The two models that were compared were the Kurucz models, which were used for this analysis, and the MARCS models. Theses models were chosen as the stellar parameters are within the limits of the models and because both models are commonly used in abundance analysis.

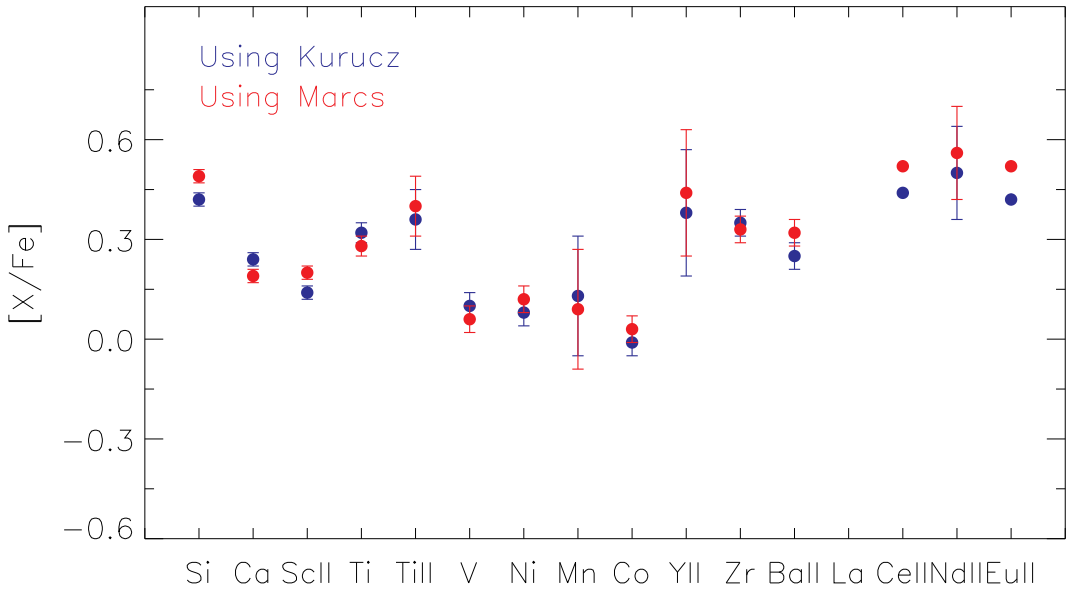

Figure 5.1 [X/Fe] abundances for Star 344 in NGC 288 derived using a Kurucz model (blue) and a MARCS model (red), using the same stellar parameters. $[\text{Fe/H}]_{\text{Kurucz}} = -1.33 \pm 0.02$ and $[\text{Fe/H}]_{\text{MARCS}} = -1.40 \pm 0.02$. The average difference between the models is 0.06 dex $\pm$ 0.03 dex.

Figure 5.1 shows that both model atmospheres result in similar [X/Fe] abundances (within 0.1 dex) and that there is no systematic abundance difference. It is therefore not likely that the atmosphere models had a great influence on the abundance errors.

5.3.2 EW measurements and the curve of growth

The EW measurements and thus the abundances are effected by undetected blends, telluric lines, and/or artefacts caused by the reduction process that can distort a spectral line. Due to the high signal-to-noise and high resolution of the spectra, these EW measurement uncertainties were greatly minimised. The major source of error in the EW measurements is the placement of the stellar continuum, and not the spectral line distortions. This error is hard to quantify, but by choosing slightly different continuum levels and noting the effects on abundance changes, it was clear that this is a major error in the EW measurements. This is the case especially for spectral lines with shorter wavelengths or lines that are in crowded parts of the spectra (Bensby et al. 2003). The semi-automated process of measuring the EWs did at no point take into account the changes in the continuum level. Another EW error which is much smaller comes from the precision by which a gaussian fit is fitted to the spectral line. This depends on the S/N and can be estimated using the relationship from Cayrel de Strobel & Spite (1988)

$$\sigma(\mathrm{EW}) \sim 1.6 \frac{\sqrt{FWHM \cdot \Delta x}}{S/N} \tag{5.1}$$

where $FWHM$ (in Å) is the width of the spectral lines, Δx is the dispersion (in Å pixel^{-1}), and S/N is the signal-to-noise ratio. Using a line of average strength (EW $\simeq$ 117.8 mÅ) at $\lambda \sim 5000$ Å ($\Delta x \simeq 0.0147$) with $FWHM = 0.16$ Å in a spectrum with $S/N = 140$ its equivalent width is measured with a precision of ~ 1.73 mÅ according to this formula, or in other words with an uncertainty of $\sim 1.5\%$.

The curve of growth (COG) is typically a log-log plot of equivalent width versus abundance. It provides a rapid way of analysing a stellar spectrum to get a first estimate of abundances and physical parameters (Villada & Rossi 1987). Every spectral line in each star has it's own COG. Although the shape of the COG changes from line to line these changes are small compared to the observational errors in EW (Gray 1992). The equation for the COG for a specific line is given as:

$$\log\left(\frac{EW}{\lambda}\right) = C + \log A + \log(gf\lambda) \tag{5.2}$$

where C is a constant. Changes in the abundance, $\log A$, are equivalent to changes in $\log(gf\lambda)$ where g is a statistical weight and f is the oscillator strength for a particular orbital.

An example of a COG can be seen in figure 5.2. Weak absorption lines have small EWs which is caused by there being few absorbing atoms. These weak absorption lines are optically thin. As the number of absorbing atoms increase the EW also increase in a linear fashion. Thus lines with small EWs are found in the initially linear part of the COG. As the number of absorbing atoms become more abundant the EWs increase. Eventually as the line center approaches a maximum amount of flux that it can absorb[2], the line bottoms out and becomes saturated. The still optically thin wings of the line continue to deepen and the line is considered optically thick. This produces little change in the lines's EW and the COG flattens out. As the abundance of the absorbing atoms increase, pressure broadening takes place causing the wings of the line to widen more rapidly. This is seen on the final part of the COG where the EWs grow more rapidly although not steeply at first (Carroll & Ostlie 2007).

By measuring EWs broader than about 150mÅ abundances were derived from the non linear part of the COG. This is shown in figure 5.2 were the 4859.74 Å Fe line with an EW of 162.8 mÅ has been placed on the line's COG. It shows that a small difference in EWs creates a large abundance difference along the flat region of the COG.

For NGC 288 59% of the Fe I lines had EWs less than 150 mÅ whilst for the case of NGC 362 this was only 37.9%. The abundance of Fe I govern the $T_{\rm eff}$of the stellar atmosphere model, thus if the Fe I EWs are inaccurate, then the model temperatures would also be inaccurate. This in turn would lead to incorrect [X/Fe] abundances since they are dependant on the EWs from the Fe I lines.

The inaccuracies in the determination of [Fe I/H] would show up in standard deviation measurements of the Fe I lines. Since NGC 362 has more Fe I lines with a EW larger than 150mÅ a larger standard deviation amongst [Fe I/H] is expected. This is indeed the case as seen in table 5.1. Furthermore when doing the photometric approach, lines with EWs larger than 150 mÅ were not included. Thus it was expected that the [Fe I/H] standard deviations would be smaller and that there ought to be hardly any difference between the clusters as they both have all their Fe I EWs less than 150 mÅ. Since almost none of the Fe II lines had EWs larger than 150 mÅ hardly any variation in the standard deviation was expected as the results in table 5.2 confirm.

Table 5.1 Average standard deviation of the [Fe I/H] abundances in the two clusters.

[Fe I/H]	$\sigma_{\rm NGC288}$	$\sigma_{\rm NGC362}$
Spectroscopic	0.17	0.18
Photometric	0.16	0.16

[2]There is always some flux received at the central wavelength.

Table 5.2 Average standard deviation of the [Fe II/H] abundances in the two clusters.

[Fe II/H]	NGC 288	NGC 362
Spectroscopic	0.15	0.15
Photometric	0.23	0.23

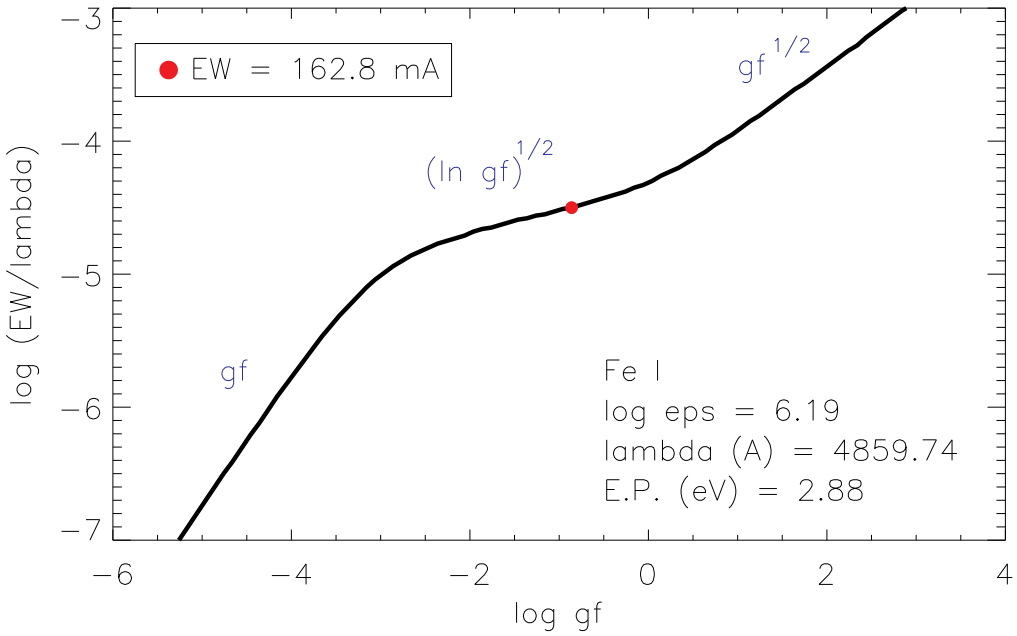

Figure 5.2 Curve of growth with $\log(\mathrm{EW}/\lambda)$ vs $\log gf$ for the Fe I line 4859.74 from star 344 in NGC 288. The red spot indicates the measured EW of the line. The black line shows the theoretical curve of growth for the spectral line with $\xi_t = 1.78$. As gf increases, the functional dependence of the EW changes. The curve of growth starts of with a linear $EW \propto gf$ relation which later turns into a $EW \propto ln(gf)^{1/2}$ relation. The curve of growth then ends with a $\sqrt{gf}$ relation.

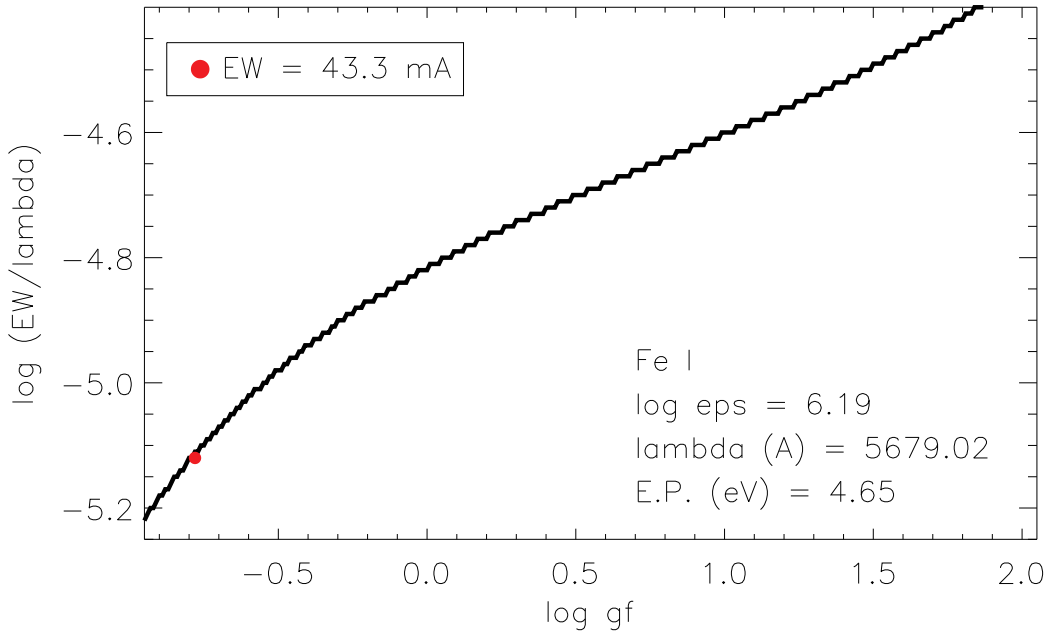

Figure 5.3 Curve of growth with $\log(\mathrm{EW}/\lambda)$ vs $\log gf$ for the Fe I line 5679.02 from star 344 in NGC 288. With a measured EW of 43.3 mÅ the measurement is well within the linear region of the curve of growth.

5.3.3 Error budget

Choosing the star 344 from NGC288 an error estimation was made based upon how much the abundances changed by changing the input parameters. The results of this is seen in table 4.15.

The error budget shows that care has to be taken when creating the models. If the an estimate of the microturbulent velocity is of by 0.3 km/s the abundance may vary of the order of 0.3 dex. Microturbulent velocity also effects the curve of growth as seen in figure 5.4. Temperature and $\log(g)$ are also very important parameters to be careful with. Metallicity effected the abundances the least.

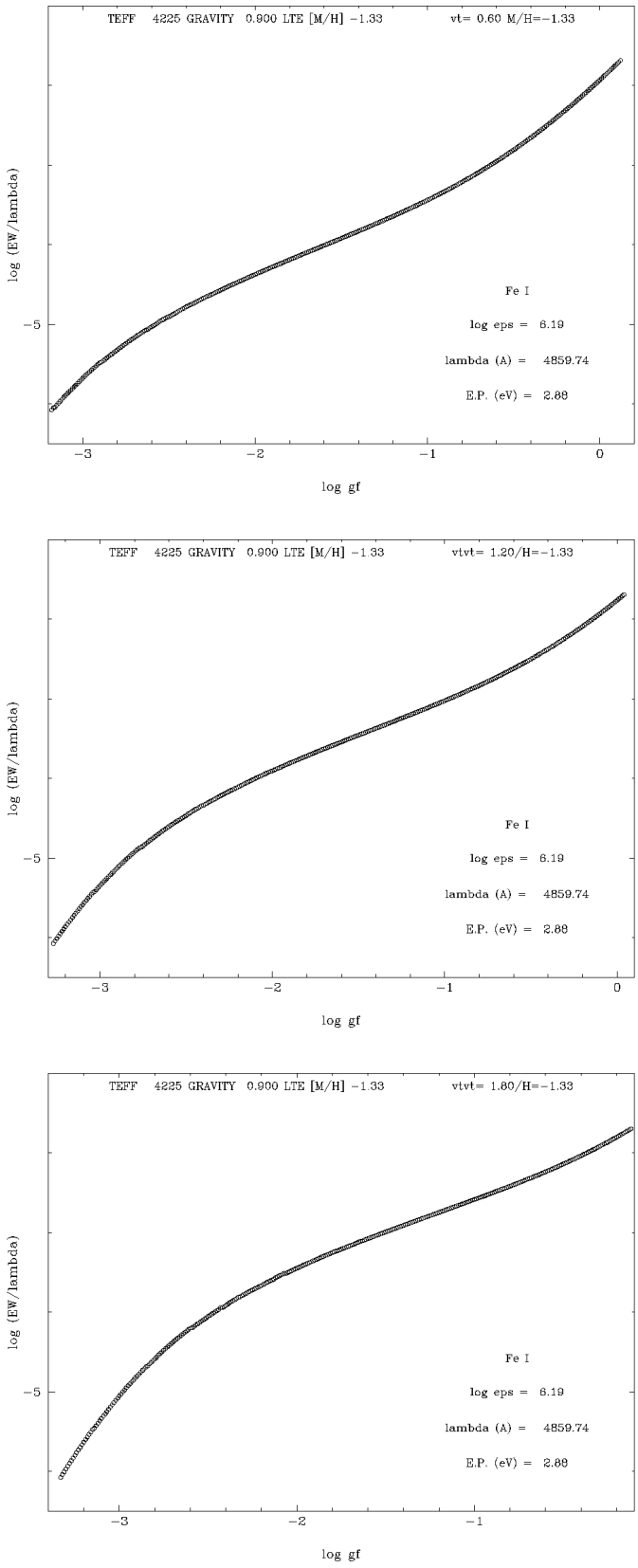

Figure 5.4 Changing curves of growth for the Fe I line 4859.74 from star 344 in NGC 288 with $\xi_t = 0.60$ in the top plot, $\xi_t = 1.20$ in the middle plot and $\xi_t = 1.80$ in the bottom plot.

5.3.4 NLTE effects

Non-LTE (NLTE) affects different lines in different ways according to the temperature. LTE was assumed when deriving all the abundances. Non-LTE effects such as overionisation by ultraviolet radiation, are known to influence certain lines such as the Fe I and Fe II lines. For sufficiently low $T_{\rm eff}$, most of the Fe will be in the form Fe I rather than Fe II. This results in incorrect stellar parameters as the the LTE analysis underestimates the amount of Fe II present in the atmosphere. This would lead to $\log(g)$ values that are to high whereas an under estimation in the amount of Fe I would result in $\log(g)$ values that are to low (Johnson 2002), (Thévenin & Idiart 1999). For higher temperature stars, Fe I is the minority species which is affected by NLTE whilst the majority Fe II is not significantly affected by the NLTE effects.

All species are affected by NLTE effects to some degree. Ti is one such element effected by NTLE. Ti I which has a lower ionisation potential than Fe I is affected before Fe I. It is likely that overionisation probably caused the high energy photons from deep layers to penetrate into the line forming regions to ionise Ti I into Ti II. With the assumption of LTE, this causes higher abundance from Ti II than corresponds to reality. Since the program stars have low stellar temperatures it is assumed that most of the Ti is in the form Ti I with Ti II being a minority species. The few high energy photons that ionise Ti I will make little overall difference to the Ti abundance as inferred from Ti I lines. However, since Ti II is a minority species, the small number of extra ionised Ti I atoms can make a large difference to the overall Ti II levels. This large difference is most likely what is observed in figures 4.1 to 4.4.

NLTE was not included in this analysis due to the sheer complexity of the calculations involved. Heavy elements have many levels and therefore require knowledge of the lifetimes and cross-sections of all the relevant transitions. Despite this there exist a number of papers which take NLTE calculations into account. For NLTE effects on Fe, Thévenin & Idiart (1999), Gehren et al. (2001), and Shchukina & Trujillo Bueno (2001) suggest corrections. For papers on NLTE effects on lighter elements, see Carlsson et al. (1994), Gratton et al. (1999) and Asplund & Lind (2010) to only mention a few.

5.3.5 Results in the context of the second parameter problem

Cohen & Meléndez (2005) found that the significantly different horizontal branch characteristics of the classic second parameter pair M3 and M13 could not be explained through differences in abundances. The reason for this, they argued, was that the two clusters have essentially identical values of [Fe/H] and of mean [X/Fe] for all of the elements they studied. Sneden et al. (2004) were also unable to explain the different HB morphologies of this second parameter pair by means of element abundances. They did suggest, however, that that the excessive blueness of the M13

HB branch is not a result of an excess He abundance. Shetrone & Keane (2000) in their analysis, concluded that NGC 288 / 362 have roughly the same abundances, α enhancement ratios, percentage of mixed stars, the same extent of deep mixing within their program stars, and no extreme mass loss taking place. Thus they provide specific suggestions towards further investigations as to the cause of the second parameter problem.

In this thesis NGC 288 and NGC 362 are found to have significantly different [Fe/H], [X/H] and [X/Fe] ratios. NGC 288 shows a greater [Fe/H] and [X/Fe] ratio, yet a smaller [X/H] ratio compared to NGC 362. Whether or not this gives any justification for the different HB locations is unclear as it is possible that these differences result from incorrect [Fe/H] determinations of NGC 362. In consideration of these results and previous work, it is clear that further investigation into the second parameter problem is required.

5.3.6 Future work

The stellar models used in this thesis are based on 1D LTE analyses. For a more accurate abundance determination, a 3D model which accounts for granulation and NLTE effects may prove to be more reliable.

Future work might also include hyperfine and/or isotopic splitting. This would lead to more accurate abundance determinations as the inferred abundances would be lower.

Another good idea would be to compare the abundances of the cluster stars to the abundances of field stars. This would give clues to the star formation history and chemical enrichment history. It would also be useful when studying abundance trends (i.e Ba/Eu or La/Eu). Further determinations of the r-process abundances by looking for Th in the spectra could confirm the proposed r-process abundances.

There is no doubt that more work has to be done determining the second parameter problem. To be able to constrain the role heavy element abundances play on the second parameter problem, theoretical work is required. With observational results from various second parameter pairs, such as the results presented in this thesis, theoretical studies which look at the heavy elements within these sorts of clusters are needed. Although heavy element abundances are unlikely to provide a solution, studies should be done to study in what way, if any, they influence the second parameter effect.

6 CONCLUSION

Presented in this thesis are the abundances of 15 heavy elements (Si to Eu) in 16 stars in the globular clusters NGC 288 and NGC 362. The overall average metalliciy ([Fe/H]) of NGC 288 is -1.40 using the spectroscopic approach and -1.33 using the photometric approach. For NGC 362 these values are -1.33 using the spectroscopic approach and -1.08 using the photometric approach. In comparison with Harris (1996), NGC 288 has a lower metallicity and NGC 362 has a higher metallicity. The average [X/Fe] ratio was higher in NGC 288 compared to NGC 362, while the [X/H] ratio showed the opposite results. The results from both the spectrometric approach and the photometric approach would suggest that NGC 362 formed from material with a higher concentration of r-process products than NGC 288. The heavy element abundances for both clusters all show strong star-to-star abundance variations for elements heavier than Sc. Since hyperfine and/or isotopic splitting have not been taken into account, the [X/Fe] measurements serve as upper limits on the element abundances in the two clusters.

The analyzed spectra, taken with UVES at the VLT, are the highest quality spectra ever obtained (R=110,000, about S/N=150) for NGC 288 and NGC 362.

Like other second parameter globular cluster pair studies by Cohen & Meléndez (2005), Shetrone & Keane (2000) and Sneden et al. (2004), it is uncertain what the role heavy element abundances play on the second parameter effect. With observational results such as those in the aforementioned papers and this thesis, theoretical studies which look at the heavy elements within these sorts of clusters would provide very useful information. Heavy element abundances are unlikely to make a big difference in providing a solution, future studies should confirm what role, if any, they have on the second parameter effect.

Studies such as the one presented in this thesis are important for providing constraints upon the uniformity of mixing in the proto-cluster environment and for constraining the role of heavy element abundance as a 2nd parameter candidate.

Appendix A

Adopted Solar Abundances

Table A.1 Adopted Solar Abundances from Asplund et al. (2009)

Species	$\log \epsilon(X)$
[Fe/H]	7.50 ± 0.04
[Fe II/H]	7.50 ± 0.04
[Si/Fe]	7.51 ± 0.03
[Ca/Fe]	6.34 ± 0.04
[Sc II/Fe]	3.15 ± 0.04
[Ti/Fe]	4.95 ± 0.05
[Ti II/Fe]	4.95 ± 0.05
[V/Fe]	3.93 ± 0.08
[Ni/Fe]	6.22 ± 0.04
[Mn/Fe]	5.43 ± 0.04
[Co/Fe]	4.99 ± 0.07
[Y II/Fe]	2.21 ± 0.05
[Zr/Fe]	2.58 ± 0.04
[Ba II/Fe]	2.18 ± 0.09
[La/Fe]	1.10 ± 0.04
[Ce II/Fe]	1.58 ± 0.04
[Nd II/Fe]	1.42 ± 0.04
[Eu II/Fe]	0.52 ± 0.04

Appendix B

Abundance calculations

In stellar astophysics, the abundance of an element is given in two forms:

B.0.7 $\log \varepsilon(X)$ notation

Abundances are expressed relative to 10^{12} hydrogen atoms:

$$\log(\text{eps}) = \log \varepsilon(X) = \log (X/\text{H}) + 12 \tag{B.1}$$

Example:

For every H atom in the sun thre are $10^{-4.5}$ iron atoms, thus
$\log \varepsilon(Fe/H) = \log \varepsilon(10^{-4.5}) = -4.5$. Substituting this into equation B.1 one finds that $\log \varepsilon(Fe) = 7.5$.

MOOG presented abundances in this notation.

B.0.8 "Bracket notation"

$$[\text{Fe/H}] = \log_{10} \left(\frac{N_{\text{Fe}}}{N_{\text{H}}} \right)_{star} - \log_{10} \left(\frac{N_{\text{Fe}}}{N_{\text{H}}} \right)_{sun} \tag{B.2}$$

This notation is also commonly used throughout this thesis for abundances of elements relative to Fe. By knowing [Eu/H], [Eu/Fe] is determined by taking the difference:

$$[\text{Eu/Fe}] = [\text{Eu/H}] - [\text{Fe/H}] \tag{B.3}$$

$$
\begin{aligned}
[\mathrm{Eu/Fe}] &= \log_{10}\left(\frac{N_{\mathrm{Eu}}}{N_{\mathrm{Fe}}}\right)_{star} - \log_{10}\left(\frac{N_{\mathrm{Eu}}}{N_{\mathrm{Fe}}}\right)_{sun} \\
&= \left(\log_{10}\left(\frac{N_{\mathrm{Eu}}}{N_{\mathrm{H}}}\right)_{star} - \log_{10}\left(\frac{N_{\mathrm{Eu}}}{N_{\mathrm{H}}}\right)_{sun}\right) \\
&- \left(\log_{10}\left(\frac{N_{\mathrm{Fe}}}{N_{\mathrm{H}}}\right)_{star} - \log_{10}\left(\frac{N_{\mathrm{Fe}}}{N_{\mathrm{H}}}\right)_{sun}\right)
\end{aligned}
$$

Bibliography

Alonso, A., Arribas, S., & Martínez-Roger, C. 1999*a*, Astron. Astrophys. Suppl. Ser., 139(2), 335–358

Alonso, A., Arribas, S., & Martínez-Roger, C. 1999*b*, A&AS, 140, 261–277

Asplund, M. & Lind, K. 2010, ArXiv e-prints

Asplund, M., Grevesse, N., Sauval, A. J., & Scott, P. 2009, ARAA, 47, 481–522

Bensby, T., Feltzing, S., & Lundström, I. 2003, A&A, 410, 527–551

Blackwell, D. E. & Shallis, M. J. 1977, MNRAS, 180, 177–191

Burbidge, E. M., Burbidge, G. R., Fowler, W. A., & Hoyle, F. 1957, Reviews of Modern Physics, 29, 547–650

Burris, D. L., Pilachowski, C. A., Armandroff, T. E., et al. 2000, ApJ, 544, 302–319

Carlsson, M., Rutten, R. J., Bruls, J. H. M. J., & Shchukina, N. G. 1994, A&A, 288, 860–882

Carroll, B. W. & Ostlie, D. A. 2007, *An Introduction to Modern Astrophysics (Second Edition)*, Addison-Wesley

Catelan, M., Bellazzini, M., Landsman, W. B., et al. 2001, AJ, 122, 3171–3182

Cayrel de Strobel, G. & Spite, M. (Eds.) 1988, *The impact of very high S/N spectroscopy on stellar physics: proceedings of the 132nd Symposium of the International Astronomical Union held in Paris, France, June 29-July 3, 1987.*, vol. 132 of *IAU Symposium*

Cohen, J. G. & Meléndez, J. 2005, AJ, 129, 303–329

Cox, A. N. & Pilachowski, C. A. 2000, Physics Today, 53(10), 100000–+

D'Antona, F., Caloi, V., Montalbán, J., Ventura, P., & Gratton, R. 2002, A&A, 395, 69–75

Dekker, H., D'Odorico, S., Kaufer, A., Delabre, B., & Kotzlowski, H. 2000, in *Society of Photo-Optical Instrumentation Engineers (SPIE) Conference Series*, M. Iye & A. F. Moorwood (Ed.), vol. 4008 of *Society of Photo-Optical Instrumentation Engineers (SPIE) Conference Series*, 534–545

Demarque, P., Lee, Y., Zinn, R., & Green, E. M. 1989, in *The Abundance Spread within Globular Clusters: Spectroscopy of Individual Stars*, G. Cayrel de Strobel (Ed.), 97–103

Demarque, P., Woo, J., Kim, Y., & Yi, S. K. 2004, ApJS, 155, 667–674

Dotter, A., Sarajedini, A., Anderson, J., et al. 2010, ASTROPHYSICAL JOURNAL, 708, 698

Gehren, T., Korn, A. J., & Shi, J. 2001, A&A, 380, 645–664

Gratton, R. G. 1987, A&A, 179, 181–192

Gratton, R. G., Carretta, E., Eriksson, K., & Gustafsson, B. 1999, A&A, 350, 955–969

Gratton, R., Sneden, C., & Carretta, E. 2004, ARAA, 42, 385–440

Gray, D. F. 1992, *The observation and analysis of stellar photospheres.*

Grundahl, F., Catelan, M., Landsman, W. B., Stetson, P. B., & Andersen, M. I. 1999, ApJ, 524, 242–261

Harris, W. 1996, AJ, 112, 1487

Johnson, J. A. 2002, ApJS, 139, 219–247

Kurucz, R. 1993, ATLAS9 Stellar Atmosphere Programs and 2 km/s grid. Kurucz CD-ROM No. 13. Cambridge, Mass.: Smithsonian Astrophysical Observatory, 1993.

Michaud, G., Vauclair, G., & Vauclair, S. 1983, ApJ, 267, 256–270

Ramírez, I. & Meléndez, J. 2005, ApJ, 626, 465–485

Rood, R. T. 1973, ApJ, 184, 815–838

Sandage, A. & Wildey, R. 1967, ApJ, 150, 469–+

Shchukina, N. & Trujillo Bueno, J. 2001, ApJ, 550, 970–990

Shetrone, M. D. & Keane, M. J. 2000, AJ, 119, 840–850

Sneden, C. 1973, ApJ, 184, 839–849

Sneden, C., Kraft, R. P., Guhathakurta, P., Peterson, R. C., & Fulbright, J. P. 2004, AJ, 127, 2162–2184

Thévenin, F. & Idiart, T. P. 1999, ApJ, 521, 753–763

Timmes, F. X., Woosley, S. E., & Weaver, T. A. 1995, ApJS, 98, 617–658

VandenBerg, D. A., Bergbusch, P. A., & Dowler, P. D. 2006, ApJS, 162, 375–387

Villada, M. & Rossi, L. 1987, Ap&SS, 136, 351–361

Wheeler, J. C., Sneden, C., & Truran, Jr., J. W. 1989, ARAA, 27, 279–349